# Force inference in granular materials: Uncertainty analysis and application to three-dimensional experiment design

Kwangmin Lee
*Department of Mechanical Engineering, Johns Hopkins University, Baltimore, Maryland 21218, USA*

Ryan C. Hurley*
*Department of Mechanical Engineering, Johns Hopkins University, Baltimore, Maryland 21218, USA*
*and Hopkins Extreme Materials Institute, Johns Hopkins University, Baltimore, Maryland 21218, USA*

(Received 14 November 2021; accepted 18 May 2022; published 27 June 2022)

Interparticle forces are known to influence mechanical and physical properties of granular materials. A method for inferring forces in two-dimensional and three-dimensional experiments has recently been developed and applied to the problem of examining force statistics, energy dissipation, fracture mechanics, and force-property relations. However, a systematic analysis of uncertainties in the forces inferred through this method has not been undertaken. In this paper, our goal is therefore to perform such a systematic analysis. We first review and modify the force inference technique to eliminate its sensitivity to the choice of units and coordinate system origin. We then use discrete-element method simulations to perform a systematic study of how experimental uncertainties and data-processing errors lead to errors in inferred forces. For the considered experiments and simulations, we find that (1) errors in inferred force magnitudes and orientations increase as the ratio between particle stress uncertainties and a measure of stress imposed on the system increases, but remain small in the largest forces in a material; (2) the absence of a moderate number of particle stress tensors in the force inference procedure leads to negligible errors in inferred force magnitudes and orientations; and (3) particle stress tensors that cannot be directly measured during experiments can be "recovered" through the force inference procedure. Based on our results, we make recommendations for future experiment design to reduce uncertainties in inferred forces.

DOI: 10.1103/PhysRevE.105.064902

## I. INTRODUCTION

Interparticle forces and force networks in granular materials have been studied extensively. Forces have been examined to understand mechanical and kinematic behavior at the grain scale [1–4], to interpret properties such as acoustic wave speeds [5,6], and to develop statistical mechanics theories [7].

Photoelastic experiments remain the most common approach for experimentally inferring interparticle forces in two-dimensional (2D) granular materials [8]. Photoelastic experiments have yielded enormous insight into force statistics and fluctuations [9,10]. Other methods for inferring forces in 2D and three-dimensional (3D) granular media have also been proposed and used in the last two decades, notably, 3D reflective index-matched scanning combined with analysis of contact areas [11,12], 3D x-ray computed tomography (XRCT) in compliant materials combined with analysis of contact areas [13], 3D confocal microscopy of emulsions combined with analysis of contact areas [14], 2D imaging of mechanoluminescent-coated particles [15], combining 2D or 3D imaging with discrete element method (DEM) simulations [16], and combining 3D XRCT with 3D x-ray diffraction (3DXRD) of stiff crystalline grains with mathematical inversion of governing balance laws [17]. While each of these methods has yielded unique insight into the structure of forces in granular media, the method combining XRCT and 3DXRD is the subject of the present paper.

Experiments combining XRCT and 3DXRD have recently been combined with a mathematical method for inferring interparticle forces in 3D granular materials containing crystalline grains [17]. These 3D experiments and the associated force inference method have been used to study structure-property relations [18,19], force-fracture criteria [20,21], contact-scale energy dissipation [22], the influence of forces on wave propagation [5], and the influence of forces on local rearrangements [23]. The force inference technique [17] has also been used in 2D experiments to study forces, validate numerical simulations, and examine the evolution of forces during dynamic loading [24–28]. Despite the widespread use of this method, a systematic analysis of uncertainties in the forces inferred through this method has not been undertaken. Analysis of such uncertainties for this method is important in light of the growing number of applications of this force inference technique, and may also be more complex than a similar analysis for many of the other methods described in the preceding paragraph, because the method being analyzed involves inferring forces through an optimization problem, rather than through a more direct measurement of contact areas or particle deformation. We note, however, that the force inference technique we analyze here is also unique in that it does not rely on any assumption of a contact law between

*rhurley6@jhu.edu

 

particles, in contrast to some other methods that employ a contact law with measurements of contact area to infer forces (e.g., [12–14]).

The goal of this paper is to perform a systematic analysis of the force inference technique recently developed and applied to 3D data [17]. The force inference method in [17], a modified form of a prior method [28,29], relies on experimental measurements of particle stress tensors (averaged within each particle), particle positions and contact locations, and particle properties. Uncertainties in each of these measurements may lead to errors in inferred forces. These uncertainties and errors have been discussed in prior work [21,29,30] but have not been systematically analyzed for their impact on interparticle forces, except for the case of uncertainties in particle stresses in [30].

Here, we first review the force inference method of [17], modifying it to eliminate its sensitivity to the choice of units and coordinate system in Sec. II. Next, in Sec. III, we systematically examine possible sources of experimental uncertainty or error arising from a combination of experimental and algorithmic limitations, including experimental noise in particle stress tensors, particles with missing stress tensors, missing contacts or contact overdetection, errors in bulk material properties, and errors in surface friction coefficients. For this paper, we use discrete element method simulations to generate ground-truth datasets for which inputs to the force inference procedure and the actual forces are known exactly. We show that, although errors in inferred force magnitudes and orientations increase as the ratio between noise in particle stress tensors and a measure of stress imposed on the material increases, errors remain small in the largest forces in a sample, suggesting that the strong force network can still be accurately characterized by force inference in three dimensions. We also notably show that in some circumstances, through the force inference procedure, stress tensors can be accurately inferred in particles for which experimental stress measurements are unavailable, providing a promising future route to analysis of datasets for which particle stress measurements are incomplete for one of several possible reasons (e.g., in [31]). Finally, in Sec. IV we use our results to compute uncertainties in forces inferred from prior experimental data described in [22] involving two granular samples containing about 900 ruby spheres studied at each of more than ten macroscopic stress states per sample. Based on our analysis, we make recommendations regarding future experiment design. In Sec. V, we provide a discussion of our results and future work. In Sec. VI we offer concluding remarks.

## II. FORCE INFERENCE TECHNIQUE

The first force inference technique applied to 3D experimental data was developed by Hurley and colleagues [17]. The technique employs linear and angular momentum balance (force and moment equilibrium), a volume-averaged stress-force relationship, and assumptions regarding repulsive forces and friction in a minimization procedure that yields all interparticle force vectors in a static granular medium. The force inference approach requires measurements of the stress tensor of each particle (averaged over each particle's volume), the locations of each particle's volume, the locations of contact points between particles, and an estimate of interparticle and particle-boundary friction coefficients. In [17], particle volumes and contact locations were furnished by 3D x-ray computed tomography measurements and particle stress tensors were furnished by 3D x-ray diffraction measurements, both made *in situ* during quasistatic deformation of crystalline grains [17] such as quartz. We direct the reader to [17,21] and the references therein for further details about these measurement techniques. The method has also been applied in two dimensions using 2D photographic imaging to furnish particle and contact locations and digital image correlation (DIC) to furnish particle stresses [24–27].

In this section, we modify the governing equations described in [17] to eliminate their sensitivity to the choice of units and coordinate system. In the previous works [17,22,26,29], the choice of units or coordinate system origin did not introduce significant errors in the inferred force because the chosen values did not disrupt the balance of weights between the governing force-balance and stress-force equations. Nevertheless, eliminating the sensitivity of the governing equations to such choices makes the force inference method more robust for future use in a variety of settings, including in scenarios in which the choice of units or coordinate system origin varies significantly from their values in prior studies. We also provide a brief comparison of the modified force inference technique with prior versions and direct the reader to Appendix B for further quantitative comparisons. The modified equations developed in this section are used in subsequent sections to systematically examine how errors in measurements lead to errors in inferred interparticle forces.

### A. Governing equations

The equations governing the mechanical equilibrium of a packing of particles include equilibrium equations and an equation relating the stresses to the interparticle forces. In this subsection, we assemble these governing equations into two linear matrix equations for an entire granular packing, the first containing force and moment balance and the second containing stress-interparticle force relations. The force inference procedure proposed in [17], and presented in slightly modified form here, simply involves selecting a set of interparticle forces for a granular packing that minimizes the nonequality of these two matrix equations when terms within the equations are obtained through potentially inexact experimental measurements.

First, we consider the equilibrium, or force and moment balance, equations. Consider the $p$th particle in a granular material that interacts with a neighboring particle $q$ at contact $i$ and a boundary at contact $j$, as shown in Fig. 1. Force and moment balance of this particle can be written as [17,30]

$$\sum_{\alpha=1}^{N_c^p} \kappa^p \boldsymbol{f}^\alpha = 0, \tag{1}$$

$$\sum_{\alpha=1}^{N_c^p} (\boldsymbol{x}^\alpha - \boldsymbol{c}^p) \times \boldsymbol{f}^\alpha = 0, \tag{2}$$

where $\alpha$ are contact point labels ranging from 1 to $N_c^p$ (the number of contacts for particle $p$), $\kappa^p$ is a weight factor of

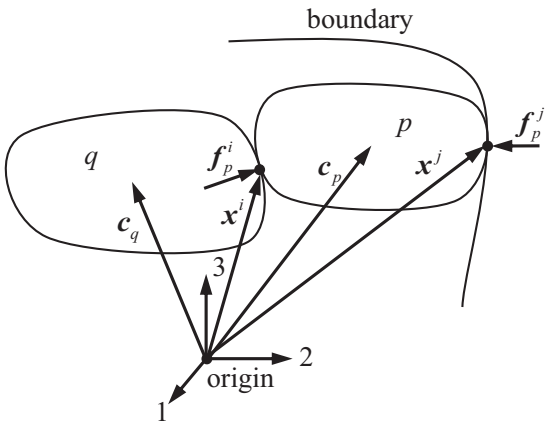


FIG. 1. Illustration of particle $p$ in contact with particle $q$ at point $i$ and with the boundary at point $j$. $\boldsymbol{c}$ vectors denote centers of mass and $\boldsymbol{f}$ vectors denote contact forces.

particle $p$, $\boldsymbol{f}^\alpha$ is the interparticle force vector at contact $\alpha$, $\boldsymbol{x}^\alpha$ is a vector from the origin of a Cartesian coordinate system to contact $\alpha$, and $\boldsymbol{c}^p$ is a vector from the origin to the center of mass of particle $p$. Equations (1) and (2) are simply a statement that particle $p$ is in force and moment equilibrium under the action of all forces at $N_c^p$ points on its boundary. In Eq. (1), the weight factor $\kappa^p$ is a scalar that is intended to eliminate the unit difference between the force balance and moment balance equations. $\kappa^p$ was absent in prior versions of the force inference technique [17,26,29] and is derived in Appendix A. The weight factor $\kappa^p$ typically takes a value close to the particle radius. In contrast to prior force inference techniques in [17,30], Eq. (2) also features $\boldsymbol{c}^p$, which makes each torque in the sum in this equation about the center of particle $p$ rather than the origin of the coordinate system. The use of $\boldsymbol{c}^p$ has the effect of making Eq. (2) independent of the origin of the coordinate system.

Equations (1) and (2) for *all particles* in a granular material can be combined in a linear matrix equation:

$$\boldsymbol{K}_{\text{eq}}\boldsymbol{f} = \boldsymbol{0}, \tag{3}$$

where $\boldsymbol{0}$ is the zero vector and

$$\boldsymbol{f} = \begin{pmatrix} \vdots \\ \boldsymbol{f}_p^i \\ \vdots \\ \boldsymbol{f}_p^j \\ \vdots \end{pmatrix}, \tag{4}$$

where $\boldsymbol{f}_p^i = (f_1^i, f_2^i, f_3^i)^T$ is the force vector at contact $i$ of particle $p$, where particle $p$ contacts another particle $q$, and $\boldsymbol{f}_p^j$ is the force vector at contact $j$, where particle $p$ contacts a boundary. For the specific example shown in Fig. 1, $\boldsymbol{K}_{\text{eq}}$ is given by

$$\boldsymbol{K}_{\text{eq}} = \begin{array}{c} \\ p \\ q \end{array} \begin{array}{c} \begin{array}{cccc} \quad & i & \quad & j \end{array} \\ \begin{pmatrix} \ddots & \boldsymbol{0} & \cdots & \boldsymbol{0} & \cdots \\ \boldsymbol{0} & \boldsymbol{k}_{eq,p}^i & \boldsymbol{0} & \boldsymbol{k}_{eq,p}^j & \boldsymbol{0} \\ \vdots & \boldsymbol{0} & \ddots & \boldsymbol{0} & \vdots \\ \boldsymbol{0} & \boldsymbol{k}_{eq,q}^i & \boldsymbol{0} & \boldsymbol{0} & \boldsymbol{0} \\ \vdots & \boldsymbol{0} & \vdots & \boldsymbol{0} & \ddots \end{pmatrix} \end{array}. \tag{5}$$

In general, the matrix $\boldsymbol{K}_{\text{eq}}$ has dimensions $6N_p \times 3N_c$ in three dimensions ($3N_p \times 2N_c$ in two dimensions), where $N_c$ is the total number of contacts in a material and $N_p$ is the total number of particles. The weights $\kappa^p$ are captured in a submatrix, e.g., $\boldsymbol{k}_{eq,p}^i$, to be defined below. The $p$ and $q$ row labels and $i$ and $j$ column labels in Eq. (5) are illustrative examples related to Fig. 1. These examples convey that a submatrix $\boldsymbol{k}_{\text{eq}}$ appears only where a particle contacts another particle or boundary; otherwise, the corresponding entries in $\boldsymbol{K}_{\text{eq}}$ are zero.

The vectors $\boldsymbol{f}$ and $\boldsymbol{0}$ in Eq. (3) each have dimensions $3N_c \times 1$ in three dimensions ($2N_c \times 1$ in two dimensions). Each submatrix within $\boldsymbol{K}_{\text{eq}}$, e.g. $\boldsymbol{k}_{eq,p}^i$, is specific to a single particle. For particle $p$ and contact $i$, this submatrix is written

$$\boldsymbol{k}_{eq,p}^i = \begin{bmatrix} \kappa^p & 0 & 0 \\ 0 & \kappa^p & 0 \\ 0 & 0 & \kappa^p \\ 0 & -\left(x_3^i - c_3^p\right) & \left(x_2^i - c_2^p\right) \\ \left(x_3^i - c_3^p\right) & 0 & -\left(x_1^i - c_1^p\right) \\ -\left(x_2^i - c_2^p\right) & \left(x_1^i - c_1^p\right) & 0 \end{bmatrix}. \tag{6}$$

Equation (3) can now be written as a statement of force and moment equilibrium for a granular packing with any number of particles and contacts.

We now consider the relationship between particle stresses and interparticle forces. The volume-averaged stress within particle $p$, $\bar{\boldsymbol{\sigma}}^p$, can be written using the linear momentum balance equation as

$$\bar{\boldsymbol{\sigma}}^p = \frac{1}{V_p}\sum_{\alpha=1}^{N_c^p}(\boldsymbol{x}^\alpha - \boldsymbol{c}^p) \otimes \boldsymbol{f}^\alpha, \tag{7}$$

where $V_p$ is the volume of the particle and the particle is assumed to be in static equilibrium. Equation (7) for *all particles* in a granular material can be combined in a linear matrix equation

$$\boldsymbol{K}_{\text{st}}\boldsymbol{f} = \boldsymbol{b}_{\text{st}}, \tag{8}$$

where $\boldsymbol{b}_{\text{st}}$ is a $6N_p \times 1$ column vector in three dimensions ($3N_p$ in two dimensions) capturing the left-hand side of Eq. (7) multiplied by the particle volume and given by

$$\boldsymbol{b}_{\text{st}} = \begin{pmatrix} \vdots \\ \boldsymbol{b}^p \\ \vdots \\ \boldsymbol{b}^q \\ \vdots \end{pmatrix}, \quad \text{where } \boldsymbol{b}_p = \begin{pmatrix} V_p\bar{\sigma}_{11}^p \\ V_p\bar{\sigma}_{22}^p \\ V_p\bar{\sigma}_{33}^p \\ 2V_p\bar{\sigma}_{23}^p \\ 2V_p\bar{\sigma}_{13}^p \\ 2V_p\bar{\sigma}_{12}^p \end{pmatrix}. \tag{9}$$

In general, the matrix $\boldsymbol{K}_{\mathrm{st}}$ has dimensions $6N_p \times 3N_c$ in three dimensions ($3N_p \times 2N_c$ in two dimensions) and for the specific case shown in Fig. 1 is given by

$$\boldsymbol{K}_{\mathrm{st}} = \begin{array}{c} \\ p \\ \\ q \\ \\ \end{array} \begin{array}{c} \begin{array}{ccccc} & & i & & j & \\ \end{array} \\ \begin{pmatrix} \ddots & \mathbf{0} & \cdots & \mathbf{0} & \cdots \\ \mathbf{0} & \boldsymbol{k}^i_{st,p} & \mathbf{0} & \boldsymbol{k}^j_{st,p} & \mathbf{0} \\ \vdots & \mathbf{0} & \ddots & \mathbf{0} & \vdots \\ \mathbf{0} & \boldsymbol{k}^i_{st,q} & \mathbf{0} & \mathbf{0} & \mathbf{0} \\ \vdots & \mathbf{0} & \vdots & \mathbf{0} & \ddots \end{pmatrix} \end{array}. \tag{10}$$

As with $\boldsymbol{K}_{\mathrm{eq}}$, each submatrix within $\boldsymbol{K}_{\mathrm{st}}$ is specific to a single particle and contact in the granular packing. In $\boldsymbol{K}_{\mathrm{st}}$, the submatrices, e.g., $\boldsymbol{k}^i_{st,p}$, are given by

$$\boldsymbol{k}^i_{st,p} = \begin{bmatrix} x^i_1 - c^p_1 & 0 & 0 \\ 0 & x^i_2 - c^p_2 & 0 \\ 0 & 0 & x^i_3 - c^p_3 \\ x^i_2 - c^p_2 & x^i_1 - c^p_1 & 0 \\ x^i_3 - c^p_3 & 0 & x^i_1 - c^p_1 \\ 0 & x^i_3 - c^p_3 & x^i_2 - c^p_2 \end{bmatrix}. \tag{11}$$

Equation (8) can now be written to relate particle stresses to interparticle forces for a granular packing with any number of particles and contacts.

As in prior work, the two matrix equations in Eqs. (3) and (8) can be employed to infer forces throughout an entire granular packing. To do this, all terms in these equations except the interparticle force vectors $\boldsymbol{f}^\alpha$ must be measured. In practice, this is possible for crystalline grains using XRCT and 3DXRD in three dimensions [17] or for a variety of grain materials using imaging and DIC in two dimensions [26]. Once these measurements are made, forces can be inferred by

$$\boldsymbol{f} = \arg\min_{\boldsymbol{f}} (\lambda |\boldsymbol{K}_{\mathrm{eq}} \boldsymbol{f}|_2 + |\boldsymbol{K}_{\mathrm{st}} \boldsymbol{f} - \boldsymbol{b}_{\mathrm{st}}|_2), \tag{12}$$

where $|\cdots|_2$ is the two-norm (which may be replaced by the one-norm, as explored in Appendix B), and the minimization can be constrained to obey Eqs. (13) and (14). The term $\lambda$ is a tradeoff parameter that may be selected to be greater than, less than, or equal to unity, depending upon whether more, less, or equal weight, respectively, is given to the equilibrium equations in comparison to the stress-interparticle force equations during minimization. Such weighting may be needed when weights within one set of equations can be measured with more accuracy than weights within the other set. In practice, we have found that a value of $\lambda = 1$ typically provides a favorable minimization of errors. We therefore adopt this value throughout the paper but explore other choices in Appendix B.

Equation (12) seeks to obtain a set of forces throughout an entire granular packing, $\boldsymbol{f}$, that minimizes the nonequality of Eqs. (3) and (8). Such nonequality arises because experimental measurements may be inexact. The use of the two-norm in our objective function is equivalent to the maximum likelihood estimate of a vector of values when Gaussian noise is present [32]. That the noise or error in experimental measurements—for instance of particle stress tensor components—can be approximated by a Gaussian distribution has been demonstrated in several prior papers [21,30].

Two constraints—one imposing repulsive forces and one limiting inferred forces by a Coulomb friction criterion—have been imposed on the minimization in Eq. (12) in prior work [17]. These constraints can be written for any contact $\alpha$ on particle $p$ as

$$\boldsymbol{e}^\alpha_p \cdot \boldsymbol{f}^\alpha_p \geqslant 0, \tag{13}$$

$$\mu \boldsymbol{e}^\alpha_p \cdot \boldsymbol{f}^\alpha_p - \sqrt{\left(\boldsymbol{t}^\alpha_{p1} \cdot \boldsymbol{f}^\alpha_p\right)^2 + \left(\boldsymbol{t}^\alpha_{p2} \cdot \boldsymbol{f}^\alpha_p\right)^2} \geqslant 0, \tag{14}$$

where $\boldsymbol{e}^\alpha_p$ is a normal vector to the contact plane at contact $\alpha$ pointing toward the interior of particle $p$, $\mu$ is the Coulomb friction coefficient, and $\boldsymbol{t}^\alpha_{p1}$ and $\boldsymbol{t}^\alpha_{p2}$ are mutually orthogonal tangent vectors and lie in the contact plane and therefore define a basis for any point within the contact plane. The vectors $\boldsymbol{t}^\alpha_{p1}$ and $\boldsymbol{t}^\alpha_{p2}$ uniquely give the tangential force magnitude through the second term on the left-hand side of Eq. (14) so long as they form a basis for the contact plane. Equations (13) and (14) can be combined into a linear constraint equation that is a statement that forces are repulsive and do not exceed the Coulomb friction criterion. This linear constraint equation can be written

$$\boldsymbol{B}\boldsymbol{f} \geqslant \boldsymbol{0}. \tag{15}$$

### B. Uniqueness and history dependence

The minimization procedure in Eq. (12) involves $12N_p$ equations in three dimensions and $6N_p$ equations in two dimensions and seeks to infer $3N_c$ force components in three dimensions and $2N_c$ force components in two dimensions. The minimization produces a unique set of forces when the number of equations exceeds the number of unknowns, or when $N_c \leqslant 4N_p$ in three dimensions and $N_c \leqslant 3N_p$ in two dimensions. For a granular material containing a sufficiently large number of particles, this constraint is satisfied for coordination numbers (contacts per particle) approaching 8 in three dimensions and 6 in two dimensions because most contacts are shared between two particles.

The minimization procedure in Eq. (12) does not take history dependence into consideration. Although interparticle forces are history dependent for a given particle packing structure, a unique set of interparticle forces can be related to a given particle packing structure when particle stresses are known and the number of equations exceeds the number of unknown force vector components, as described in the previous paragraph. In this paper and in previous applications of the force inference method, the granular materials of interest always satisfy the uniqueness criterion imposed by having more equations than unknowns [17,19,22]; exceptions to this are noted explicitly throughout the paper (e.g., in Sec. III F).

### C. Units and origin in the minimization process

The governing equations in Sec. II A are modified from those present in prior work (e.g., [17]). In particular, Eq. (6) for $\boldsymbol{k}^\alpha_{eq,p}$ contains a constant $\kappa^p$ with units of length that was absent in prior work and is included here to ensure that all equations captured in Eq. (3) have units of length $\times$ force.

TABLE I. Force inference methods.

| Method | Feature | Minimization |
|---|---|---|
| 1[a] | Depends on unit of length and origin | $\boldsymbol{f} = \arg\min(\lvert\boldsymbol{K}_{\mathrm{st}}\boldsymbol{f} - \boldsymbol{b}_{\mathrm{st}}\rvert_2)$ subject to $\boldsymbol{K}_{\mathrm{eq}}\boldsymbol{f} = 0$ and $\boldsymbol{B}\boldsymbol{f} \geqslant \boldsymbol{0}$ |
| 2[b] | Depends on unit of length and origin | $\boldsymbol{f} = \arg\min(\lambda\lvert\boldsymbol{K}_{\mathrm{eq}}\boldsymbol{f}\rvert_2 + \lvert\boldsymbol{K}_{\mathrm{st}}\boldsymbol{f} - \boldsymbol{b}_{\mathrm{st}}\rvert_2)$ with $\lambda = 0.1, 1, 10$ subject to $\boldsymbol{B}\boldsymbol{f} \geqslant \boldsymbol{0}$ |
| 3[c] | Insensitive to unit of length and origin | $\boldsymbol{f} = \arg\min(\lambda\lvert\boldsymbol{K}_{\mathrm{eq}}\boldsymbol{f}\rvert_j + \lvert\boldsymbol{K}_{\mathrm{st}}\boldsymbol{f} - \boldsymbol{b}_{\mathrm{st}}\rvert_j)$ $\lambda = 1$ and $j = 1, 2$ subject to $\boldsymbol{B}\boldsymbol{f} \geqslant \boldsymbol{0}$ |

[a]From [29]. Note: $\boldsymbol{K}_{\mathrm{st}}$ and $\boldsymbol{K}_{\mathrm{eq}}$ do not contain $\boldsymbol{c}$ and $\kappa^p$ as in Sec. II A.
[b]From [17]. Note: $\boldsymbol{K}_{\mathrm{st}}$ and $\boldsymbol{K}_{\mathrm{eq}}$ do not contain $\boldsymbol{c}$ and $\kappa^p$ as in Sec. II A.
[c]From Sec. II A.

In contrast to prior force inference methods, Eqs. (3) and (8) both contain units of length × force. The value of $\kappa^p$ may be chosen by considering the geometry of the particles in a material to ensure that the two objective functions in Eq. (12) have similar weights. A new, detailed process for calculating $\kappa^p$ is given in Appendix A. $\kappa^p$ generally takes a value close to the radius of the particles in a granular material.

Another modification of the governing equations in Sec. II A is the consideration of vectors $\boldsymbol{c}^p$ pointing from the origin of the Cartesian coordinate system to the center of mass of the particle $p$ under consideration. This term was also absent in Eqs. (2) and (7) in prior work. The addition of this term ensures that the moment balance and stress-force relations are insensitive to the location of the origin of the coordinate system used in analysis. For instance, for moment balance in Eq. (2), including $\boldsymbol{c}^p$ ensures that moments of similar magnitudes on separate particles have similar weights in the minimization process, whereas having a coordinate system closer to one particle than another would increase the weight associated with the farthest particle in the minimization. A quantitative comparison of force inference using the modified equations in this section and those from prior work is provided in Appendix B.

### D. Summary of force inference methods

Table I summarizes the force inference methods proposed in prior work [17,29] and in Sec. II A. The primary differences in the methods are the choice of equations and weights used in the minimization function. The method proposed in this paper is the only one, through the use of $\boldsymbol{c}$ and $\kappa^p$ in $\boldsymbol{K}_{\mathrm{st}}$ and $\boldsymbol{K}_{\mathrm{eq}}$, to be insensitive to the unit of length and origin of the coordinate system used in analysis.

## III. ERROR PROPAGATION AND FORCE UNCERTAINTY

In this section, we study how experimental errors or noise, stemming from either inaccurate measurements, experimental resolution limits, or algorithmic limitations, propagate through the minimization procedure described in Sec. II A and lead to errors in inferred forces. This study is a more thorough version of those undertaken in [29,30] which consider older versions of the force inference technique or are restricted to studying the effects of noise in experimentally measured particle stresses only. The present paper is based on discrete element method simulations which generate "ground-truth" data—i.e., data for which inputs to the force inference procedure and the true forces are known exactly. Because multiple measurement errors may occur simultaneously in real experiments, the effect of multiple measurement errors on inferred forces is analyzed. The new force inference method of Sec. II A is used to evaluate the magnitude of errors present in prior studies (e.g., [5,18,19,22,26]) and make recommendations for future experiment design.

### A. Sources of error

Table II details the measurements needed in the minimization procedure explained in Sec. II A, describes whether errors in those measurements arise due to experimental limitations (labeled Expt.) or algorithmic limitations (labeled Alg.), and provides an approximate magnitude of the error. We investigate the effect of a subset of these errors on inferred force magnitudes and orientations in later subsections.

The first set of errors in Table II includes errors in particle stress tensors, $\bar{\boldsymbol{\sigma}}^p$, in Eq. (7). In 3D experiments, these are calculated in crystalline particles by first computing the average strain tensor, $\bar{\boldsymbol{\epsilon}}^p$, of each particle from 3DXRD measurements (see [17,33]). Errors in $\bar{\boldsymbol{\epsilon}}^p$ arise because of both the resolution limits of 2D area detectors used in 3DXRD measurements and algorithmic limitations within existing 3DXRD analysis codes [33,34]. The errors have been quantified in quartz and

TABLE II. Sources of errors or noise in the measurements needed in Sec. II A to perform force inference. Experimental errors are denoted by Expt.; algorithmic errors are denoted by Alg.

| Error source | Expt. | Alg. | Magnitude |
|---|---|---|---|
| Particle stress tensor[a] | ✓ | ✓ | $5 \times 10^{-5}$–$10^{-4}$ in $\boldsymbol{\epsilon}$ |
| Missing stress tensor | ✓ | ✓ | |
| Contact location | ✓ | ✓ | <1 pixel |
| Missing or extra contacts | ✓ | ✓ | |
| Particle center location | ✓ | ✓ | <1 pixel |
| Particle stiffness | ✓ | | <1% |
| Particle or wall friction | ✓ | | Unknown |

[a]Errors arise due to errors in strain, which are inferred through 3DXRD analysis and subsequently used to compute stresses.

ruby particles with diameters ranging from 100 to 300 $\mu$m as $10^{-4}$ for on-diagonal components of $\bar{\boldsymbol{\epsilon}}^p$ and $5\times10^{-5}$ for off-diagonal components of $\bar{\boldsymbol{\epsilon}}^p$ [21,30]. These values represent the standard deviation of normal distributions with mean zero. For quartz particles, this error in strain (through Hooke's law, $\bar{\boldsymbol{\sigma}}^p = \mathbb{C} : \bar{\boldsymbol{\epsilon}}^p$, where $\mathbb{C}$ is the elastic stiffness tensor) leads to "noise" in stresses of 10 and 5 MPa for on- and off-diagonal components of $\bar{\boldsymbol{\sigma}}^p$ [21]. For ruby or sapphire particles, the noise in stresses is 50 and 23 MPa, respectively, for on- and off-diagonal components of $\bar{\boldsymbol{\sigma}}^p$ (see [30]). Therefore, the noise of on- and off-diagonal stress components can be approximately represented as $E\times10^{-4}$ and $E\times5\times10^{-5}$, respectively, where $E$ is Young's modulus of materials. We note that this magnitude of noise is independent of experimental boundary conditions, including boundary stresses. Rather, it is intrinsic to the material being studied and the experimental resolution and algorithms. To make the magnitude of this noise meaningful in the analysis performed later in this paper, we will typically divide it by a measure of average trace of all particle stress tensors when we examine its effects in Sec. IV B. In 2D experiments, errors in particle stress tensors may also arise because of camera resolution limitations and algorithmic limitations of DIC codes [26,29]. These errors in particle stress tensors are also typically fixed in their magnitude of strain for a given imaging system and speckle pattern [35], and therefore depend on the material being studied.

The second set of errors in Table II is missing stress tensors. Three-dimensional granular systems studied using 3DXRD analysis may suffer from missing or overlapping diffraction peaks for certain particles due to the dynamic range of area detectors or particle fracture (e.g., [20,21]). If the number of missing peaks falls below a user-defined threshold, the particles will not be assigned a stress tensor. In 2D granular systems, poor correlation of DIC windows may also lead to inaccurate or absent average stress results for specific particles.

The third set of errors in Table II includes errors in the locations of particle-particle or particle-boundary contacts, $\boldsymbol{x}^\alpha$ in Eqs. (1), (2), and (7). Such errors may arise because of both the resolution limits of XRCT images and the selection of parameters in image-processing algorithms used for image segmentation and contact detection [36,37]. We estimate that, if present, these errors are less than the length of 1 pixel (in 3D XRCT images or 2D images) in standard deviation and have mean zero. This estimate is based on our observation that contact points obtained by typical 3D analysis approaches (e.g., [20]) are typically composed of many pixels. Averaging the location of many pixels typically results in an error less than the size of a single pixel [38]. Because errors in contact locations are assumed to be small, we do not investigate their influence on inferred forces here.

The fourth set of errors in Table II is missing interparticle or particle-boundary contacts or contact overdetection. Either of these errors may arise due to image resolution and limitations in contact detection algorithms in two and three dimensions (see [37] for a discussion of these errors).

The fifth set of errors in Table II includes errors in the locations of particle centers, $\boldsymbol{c}^p$, in Eqs. (2) and (7). These errors arise for similar reasons as errors in contact locations. Prior work has estimated that the magnitude of these errors may be significantly less than the length of a pixel in XRCT images (perhaps as low as 0.05% of the pixel size) [38]. We therefore do not investigate the influence of these errors on inferred forces here.

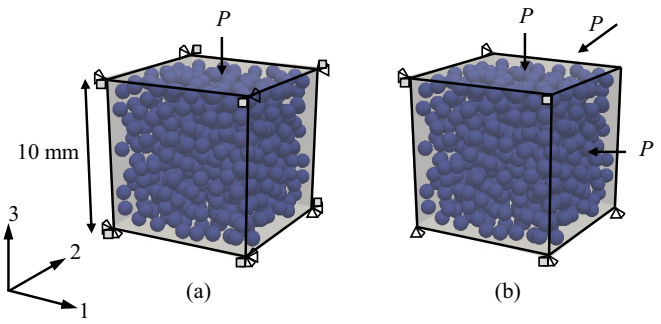


FIG. 2. DEM geometry of (a) uniaxial and (b) triaxial compression test on a cubic material (edge length is 10 mm).

The sixth and seventh sets of error in Table II are errors in particle stiffness and particle-particle or particle-wall friction coefficients. Errors in these quantities arise because of natural material variability and errors in calibration experiments performed with the objective of characterizing material elasticity or friction coefficients. When experiments are performed with crystalline grains in three dimensions, as in our prior work, particle moduli are assumed to be very accurate because the crystal lattice parameters can be directly quantified and compared with existing literature. Any errors in particle stiffness are therefore assumed to be captured in the first set of errors—those related to particle stress tensors. When experiments are performed in two dimensions (e.g., in [26,29]), particle moduli deviate by several percent of their characterized values due to resolution limitations of characterization experiments or the nonlinear elastic response of the frequently used polymeric particles. In both 3D and 2D experiments, the interparticle and particle-boundary friction coefficients may deviate significantly from their expected values due to surface roughness, aging, or variability under normal compression (e.g., [39]). Further experiments are needed to quantify this friction variability for particles frequently used in granular mechanics studies.

### B. Discrete element method study

A 3D DEM model of uniaxial and triaxial compression is used to generate ground-truth datasets in which all inputs to the force inference procedure of Sec. II A and all resulting forces are known exactly. The DEM code used for this is LIGGGHTS (version 3.8.0) [40]. Figure 2 shows the geometry of the uniaxial and triaxial compression tests. A simulation box is created using analytically defined and meshed walls. Simulations shown in Fig. 2 employ 591 spherical particles which are inserted into the simulation domain without overlap via a Monte Carlo approach (through the LIGGGHTS command "insert/pack") [40]. Increasing the number of particles up to 2500 does not significantly quantitatively affect any results regarding inferred force errors described in subsequent sections. Particles are given the properties listed in Table III. Particle sizes, density, Poisson's ratio, and friction coefficient are similar to those in experiments performed on quartz. The

TABLE III. Mechanical and contact properties of particles in DEM simulations.

| Property | Value |
|---|---|
| Particle radius (mm) | 0.5 |
| Particle density (kg/m$^3$) | 2500 |
| Number of particles | 591 |
| Young's modulus (GPa) | 1 |
| Poisson's ratio | 0.2 |
| Coefficient of restitution | 0.1 |
| Particle-particle friction coefficient | 0.4 |
| Particle-boundary friction coefficient | 0.0 |

particle Young's modulus is lower than that in experiments; however, simulations with Young's modulus up to 500 GPa do not significantly quantitatively influence results regarding inferred force errors described in subsequent sections. Modeling bidisperse granular packings with a large to small particle radius ratio of 1.4 also does not significantly quantitatively influence results of subsequent sections. After particle initialization, the walls of the simulation box are either fixed or moved according to a stress-controlled integration scheme to enforce boundary conditions on the sample. All particle-particle and particle-wall interactions are governed by a Hertzian contact model with tangential springs and a Coulomb friction criterion for sliding (the "Hertz Tangential History" contact model [40]). In the uniaxial simulation, a constant pressure, $P$, acting in the $-x_3$ direction is imposed on the wall at the $+x_3$ edge of the simulation box. In the triaxial simulation, a constant pressure, $P$, acting in the $-x_1$, $-x_2$, and $-x_3$ directions is imposed on the walls at the $+x_1$, $+x_2$, and $+x_3$ edges, respectively, of the simulation box. $P$ is chosen as 0.1, 0.5, and 1 MPa. Particles are integrated according to a velocity-Verlet scheme and gravity is ignored in all calculations. Walls are controlled by the "Mesh Surface Stress Servo" command.

The macroscopic stress-strain and coordination-strain curves for the 1.0-MPa uniaxial and triaxial tests are shown in Figs. 3(a) and 3(b), respectively. The hydrostatic stress in Fig. 3(b) is given by $\sigma_v = (\sigma_{11} + \sigma_{22} + \sigma_{33})/3$ and the volumetric strain is given by $\epsilon_v = \epsilon_{11} + \epsilon_{22} + \epsilon_{33}$. Both Figs. 3(a) and 3(b) illustrate that the average coordination number increases monotonically with applied hydrostatic stress on the sample. Table IV contains, for all six DEM simulations, the standard deviation of normalized force magnitudes for all contacts, von Mises stress for all particles, and average coordination number for all particles. The standard deviation of force magnitudes and von Mises stresses decrease with applied sample stress, consistent with a more negative exponent of force magnitude decay for larger macroscopic stresses [17]. The average coordination number does increase monotonically with applied sample stress. Figure 4 shows the probability density of normalized force magnitude, $p(f^\alpha/\langle f^\alpha\rangle)$, and probability density of normalized von Mises stress, $p(\bar{\sigma}^p_{vm}/\langle\bar{\sigma}^p_{vm}\rangle)$, for all simulations.

TABLE IV. The standard deviation of normalized contact force, std$(f^\alpha/\langle f^\alpha\rangle)$, von Mises stress, std$(\bar{\sigma}^p_{vm}/\langle\bar{\sigma}^p_{vm}\rangle)$, and average coordination number, $n$, for all six DEM simulations.

| Experiment | std$(f^\alpha/\langle f^\alpha\rangle)$ | std$(\bar{\sigma}^p_{vm}/\langle\bar{\sigma}^p_{vm}\rangle)$ | $n$ |
|---|---|---|---|
| Uniaxial, 0.1 MPa | 0.61 | 0.41 | 4.91 |
| Uniaxial, 0.5 MPa | 0.65 | 0.41 | 5.19 |
| Uniaxial, 1.0 MPa | 0.58 | 0.31 | 5.49 |
| Triaxial, 0.1 MPa | 0.35 | 0.23 | 5.09 |
| Triaxial, 0.5 MPa | 0.27 | 0.13 | 5.67 |
| Triaxial, 1.0 MPa | 0.22 | 0.11 | 5.94 |

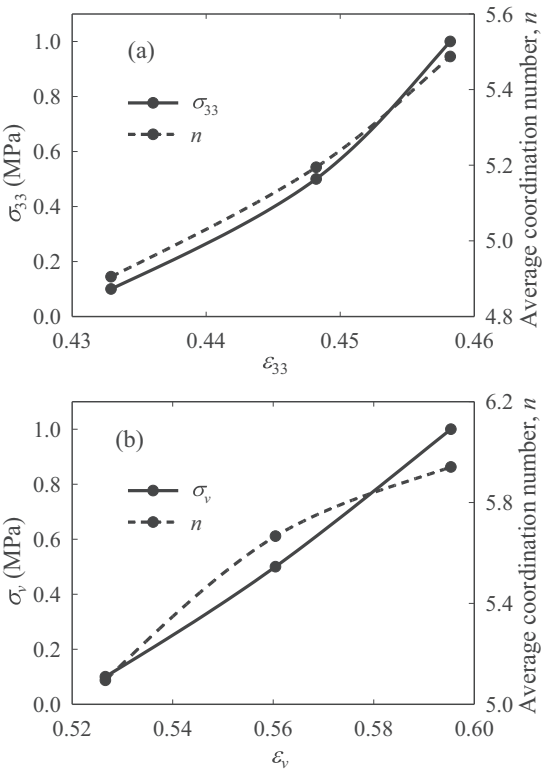


FIG. 3. Sample stress-strain curve and coordination-strain curve for (a) the 1.0-MPa uniaxial compressive test and (b) the 1.0-MPa triaxial compressive test.

### C. Force inference validation with ground-truth data

Force vectors at each interparticle contact are known exactly from DEM simulations. These force vectors are used in Eq. (7) to compute the ground-truth stress tensors for each particle. When these ground-truth stresses and the particle volume and contact position information are used in Eq. (12), forces are inferred without any errors, as in [30]. The number of equations used in the minimization procedure, equal to the sum of the number of rows in $\boldsymbol{K}_{\rm st}$ and $\boldsymbol{K}_{\rm eq}$, is 7092, while the number of unknown force vector components ranges between 4767 and 4944 for the 0.1-MPa DEM simulations and 5316 and 5724 for the 1.0-MPa DEM simulations. The minimization procedure in Eq. (12) is therefore overconstrained and the observation that forces are inferred exactly and without errors is expected.

### D. Definition of error measures

To clearly describe errors in inferred forces, we first define error measures in this subsection and summarize them in

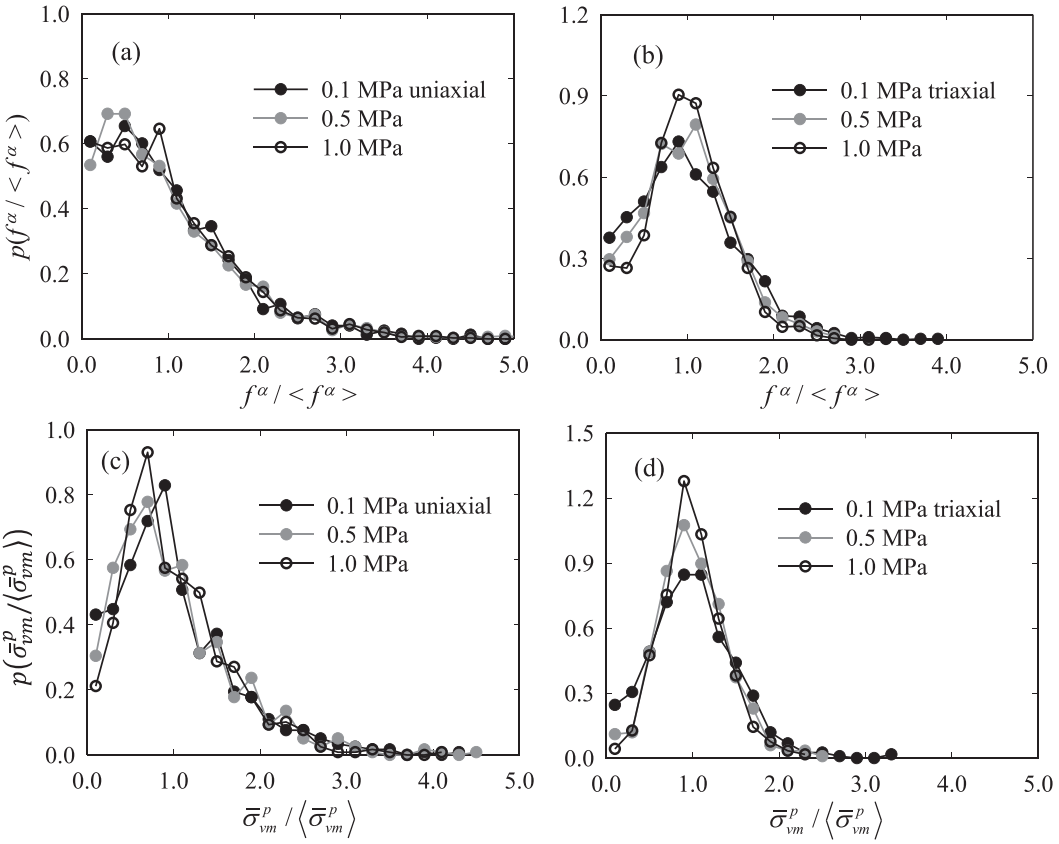


FIG. 4. Average normalized force magnitude distributions for (a) uniaxial and (b) triaxial simulations. Average normalized von Mises stress distributions for (c) uniaxial and (d) triaxial simulations.

Table V. We label the ground-truth force vector obtained from Eq. (12) in the absence of any errors as $\boldsymbol{f}_{\mathrm{GT}}$. The force vector obtained from Eq. (12) in the presence of any sources of error from Table II is simply labeled $\boldsymbol{f}$. The ground-truth force vector, magnitude, and normal force magnitude at contact $\alpha$ are labeled $\boldsymbol{f}^\alpha_{\mathrm{GT}}$, $f^\alpha_{\mathrm{GT}}$, and $f^\alpha_{n,\mathrm{GT}}$ respectively. The force vector, magnitude, and normal force magnitude obtained at contact $\alpha$ in the presence of any source of error are labeled $\boldsymbol{f}^\alpha$, $f^\alpha$, and $f^\alpha_n$, respectively. The first error measure we define is the error in inferred force magnitude at $\alpha$:

$$f^\alpha_e = \left| f^\alpha - f^\alpha_{\mathrm{GT}} \right|. \tag{16}$$

We often examine $f^\alpha_e$ in its form in Eq. (22) in which an absolute value appears; however, we also examine the error without an absolute value, which we term the signed error in inferred force magnitude at $\alpha$:

$$f^\alpha_{se} = f^\alpha - f^\alpha_{\mathrm{GT}}. \tag{17}$$

We also define the error in inferred normal force magnitude at $\alpha$ as

$$f^\alpha_{n,e} = \left| f^\alpha_n - f^\alpha_{n,\mathrm{GT}} \right|, \tag{18}$$

TABLE V. Error measures.

| Name | Definition |
|---|---|
| Error in inferred force magnitude | $f^\alpha_e = \lvert f^\alpha - f^\alpha_{\mathrm{GT}} \rvert$ |
| Signed error in inferred force magnitude | $f^\alpha_{se} = f^\alpha - f^\alpha_{\mathrm{GT}}$ |
| Error in inferred normal force magnitude | $f^\alpha_{n,e} = \lvert f^\alpha_n - f^\alpha_{n,\mathrm{GT}} \rvert$ |
| Signed error in inferred normal force magnitude | $f^\alpha_{n,se} = f^\alpha_n - f^\alpha_{n,\mathrm{GT}}$ |
| Normalized error in inferred force magnitude | $f^\alpha_{e,n} = \lvert f^\alpha - f^\alpha_{\mathrm{GT}} \rvert / \langle f^\alpha_{\mathrm{GT}} \rangle$ |
| Average normalized error in inferred force magnitude | $f_e = ((1/N_c) \sum_{i=\alpha}^{N_c} f^\alpha_e) / \langle f^\alpha_{\mathrm{GT}} \rangle$ |
| Error in inferred force direction | $\theta^\alpha_e = \cos^{-1}(\boldsymbol{f}^\alpha_{\mathrm{GT}} \cdot \boldsymbol{f}^\alpha / (\lvert \boldsymbol{f}^\alpha_{\mathrm{GT}} \rvert_2 \lvert \boldsymbol{f}^\alpha \rvert_2))$ |
| Average error in inferred force direction | $\theta_e = (\sum_{i=\alpha}^{N_c} \theta^\alpha_e)/N_c$ |
| Average normalized error in inferred stress | $\sigma^e_{ij} = (\sum_{\alpha=1}^{N_p} \lvert \sigma^{\alpha,\mathrm{GT}}_{ij} - \sigma^\alpha_{ij} \rvert) / (\sum_{\alpha=1}^{N_p} \lvert \sigma^{\alpha,\mathrm{GT}}_{ij} \rvert)$ |

and the signed error in inferred normal force magnitude at $\alpha$ as

$$f^{\alpha}_{n,se} = f^{\alpha}_{n} - f^{\alpha}_{n,\mathrm{GT}}. \tag{19}$$

The error $f^{\alpha}_{e}$ can be normalized by the average ground-truth force throughout a granular packing to give the normalized error in inferred force magnitude,

$$f^{\alpha}_{e,n} = \frac{\left|f^{\alpha} - f^{\alpha}_{\mathrm{GT}}\right|}{\langle f^{\alpha}_{\mathrm{GT}}\rangle} \tag{20}$$

where

$$\langle f^{\alpha}_{\mathrm{GT}}\rangle = \frac{1}{N_c}\sum_{i=\alpha}^{N_c} f^{\alpha}_{\mathrm{GT}}, \tag{21}$$

and $\langle\cdot\rangle$ therefore represents an average calculation. The average normalized force magnitude error is given by

$$f_e = \frac{1}{N_c}\frac{\sum_{i=\alpha}^{N_c} f^{\alpha}_{e}}{\langle f^{\alpha}_{\mathrm{GT}}\rangle}. \tag{22}$$

The error in inferred force direction at contact $\alpha$ is given by

$$\theta^{\alpha}_{e} = \cos^{-1}\left(\frac{\boldsymbol{f}^{\alpha}_{\mathrm{GT}}\cdot\boldsymbol{f}^{\alpha}}{\left|\boldsymbol{f}^{\alpha}_{\mathrm{GT}}\right|_2\left|\boldsymbol{f}^{\alpha}\right|_2}\right). \tag{23}$$

The average error in inferred force direction is

$$\theta_e = \frac{\sum_{i=\alpha}^{N_c}\theta^{\alpha}_{e}}{N_c}. \tag{24}$$

The inferred stresses obtained from $\boldsymbol{K}_{\mathrm{st}}\boldsymbol{f}$, where $\boldsymbol{f}$ are the inferred forces [see Eq. (8)], can be written as $\sigma^{\alpha}_{ij}$ in index notation. The ground-truth stresses can be written $\sigma^{\alpha,\mathrm{GT}}_{ij}$. These ground-truth stresses can be obtained from Eq. (8) ($\boldsymbol{K}_{\mathrm{st}}\boldsymbol{f}_{\mathrm{GT}}$) using the ground-truth forces, $\boldsymbol{f}_{\mathrm{GT}}$. The average normalized error in inferred stresses is given by

$$\sigma^{e}_{ij} = \frac{\sum_{\alpha=1}^{N_p}\left|\sigma^{\alpha,\mathrm{GT}}_{ij} - \sigma^{\alpha}_{ij}\right|}{\sum_{\alpha=1}^{N_p}\left|\sigma^{\alpha,\mathrm{GT}}_{ij}\right|}. \tag{25}$$

### E. Errors in the particle stress tensors

The first set of errors we investigate includes errors (also interchangeably called noise) in particle stress tensors. To investigate the influence of this error on inferred forces, we draw synthetic errors from Gaussian distributions and add them to the ground-truth stresses obtained from DEM. For each particle in the DEM simulation we draw a distinct error for each on-diagonal stress tensor component from a Gaussian distribution with mean zero and standard deviation $E\times10^{-4} = 0.1$ MPa, where $E$ is the particle Young's modulus from Table III. We repeat this for each off-diagonal stress tensor component, drawing such errors from a Gaussian distribution with mean zero and standard deviation $E\times5\times10^{-5} = 0.05$ MPa. We then perform the minimization in Sec. II A using the exact results from DEM simulations for all quantities except particle stress tensors, which have the errors just described.

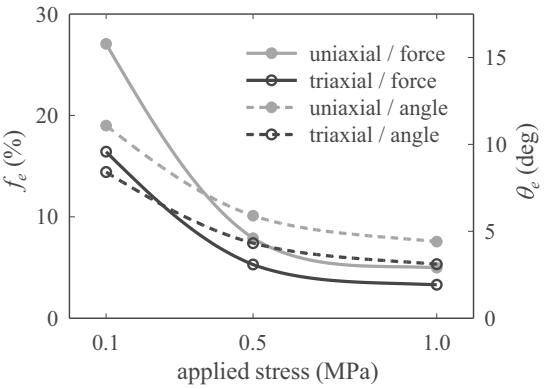


FIG. 5. (a) Average normalized inferred force magnitude error as a percentage, $f_e\times100\%$, and (b) average orientation error, $\theta_e$, for the case when noise is introduced in the particle stress tensors as described in Sec. III E.

Figure 5 illustrates the average normalized inferred force magnitude error, $f_e$, as a percentage ($f_e\times100\%$) and the average orientation error, $\theta_e$. Both errors are plotted as a function of applied stress in the DEM simulations. In all cases, $f_e$ and $\theta_e$ are smaller for triaxial compression simulations than they are for uniaxial compression simulations. Both magnitude and orientation errors are observed to decrease monotonically with increasing applied stress. This occurs because as applied macroscopic stress increases the average interparticle force increases while the standard deviation of noise in stress tensor components remains constant. This also occurs in experiments with 3DXRD measurements in three dimensions or digital image correlation measurements in two dimensions: the noise is a function of experimental resolution and inherent particle properties but is independent of the magnitude of stress in a particle.

Figure 6 conveys the average inferred force magnitude and orientation errors as a function of the ground-truth force at specific contacts. The ground-truth force magnitudes were binned and counted between integer multiples of $f^{\alpha}_{\mathrm{GT}}/\langle f^{\alpha}_{\mathrm{GT}}\rangle$ (e.g., between $f^{\alpha}_{\mathrm{GT}}/\langle f^{\alpha}_{\mathrm{GT}}\rangle = 1$ and 2) in making this figure. Figure 6(a) shows that neither the force magnitude errors nor the normalized force magnitude errors ($f^{\alpha}_{e}$ or $f^{\alpha}_{e,n}$) depend significantly on the magnitude of ground-truth force at specific contacts. The largest contact forces, such as those with $f^{\alpha}_{\mathrm{GT}}/\langle f^{\alpha}_{\mathrm{GT}}\rangle \approx 5$, have the same magnitude of error as the smallest, such as those with $f^{\alpha}_{\mathrm{GT}}/\langle f^{\alpha}_{\mathrm{GT}}\rangle \approx 0.5$, within a given simulation. We note that this indicates that $f_e$, as a function of ground-truth force, *is less* on average for individual contacts supporting larger forces than for those supporting smaller forces. Figure 6(a) shows that the average (non-normalized) error in inferred force magnitude, $f_e\times\langle f^{\alpha}_{\mathrm{GT}}\rangle$, increases as applied stress increases even if the magnitude of the noise is fixed, although the increase of $f_e\times\langle f^{\alpha}_{\mathrm{GT}}\rangle$ is small compared to the increase of applied stress. On the other hand, the error in inferred force direction, $\theta^{\alpha}_{e}$, decreases as the inferred force magnitude increases at a specific contact, as shown in Fig. 6(b).

Figure 7 shows the probability density of signed normalized inferred force magnitude errors, $p(f^{\alpha}_{se}/\langle f^{\alpha}_{e}\rangle)$, and the probability density of signed normalized inferred

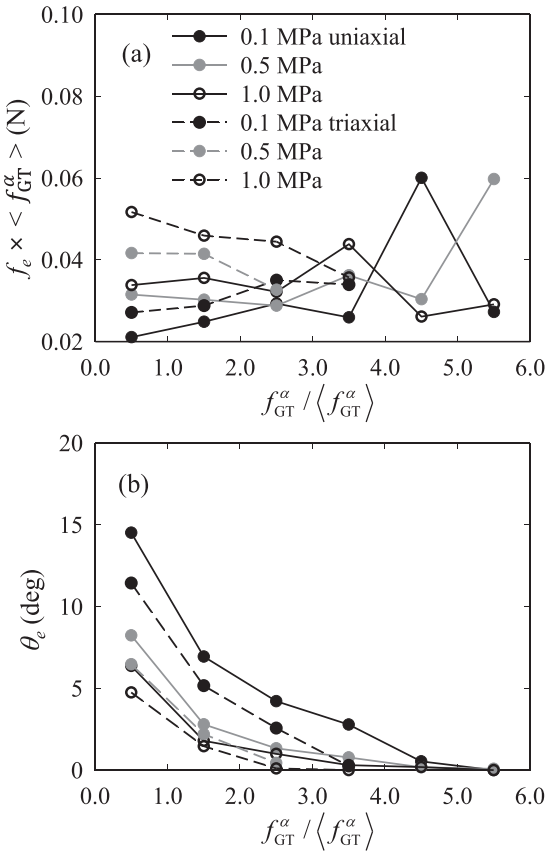


FIG. 6. Distributions of (a) average (non-normalized) inferred force magnitude error, $f_e \times \langle f^{\alpha}_{GT} \rangle$, and (b) average orientation error, $\theta_e$, for the case when noise is introduced in the particle stress tensors as described in Sec. III E.

normal force magnitude errors, $p(f^{\alpha}_{n,se}/\langle f^{\alpha}_{n,e} \rangle)$. In both uniaxial and triaxial tests, the probability densities follow a normal distribution with mean zero and a standard deviation of approximately 1.2. These values were obtained for each simulation by a least-squares fit of a Gaussian distribution with mean zero to the data points shown in Fig. 7 for the corresponding experiment.

Figure 8 illustrates the probability density of normalized inferred force magnitude errors, $p(f^{\alpha}_{e,n})$, and the probability density of inferred force direction errors, $p(\theta^{\alpha}_{e})$, for the uniaxial and triaxial DEM simulations. Figure 8 shows that both $f^{\alpha}_{e,n}$ and $\theta^{\alpha}_{e}$ decay steeply with increasing inferred force magnitude and orientation errors. This is consistent with the observation in Fig. 6 that the magnitude of force errors is insensitive to the ground-truth force magnitude at specific contacts. This result was also found in the study of measurement uncertainties in [30].

Figure 9 illustrates the average normalized error in inferred particle stresses as a percentage ($\sigma^{e}_{ij} \times 100\%$) for all particles in the uniaxial and triaxial compression simulations. Comparing $f_e$ and $\sigma^{e}_{ij}$ in Figs. 5 and 9, we find that $\sigma^{e}_{ij}$ follows a similar trend as $f_e$, and $\sigma^{e}_{ij}$ is slightly greater (by a factor between 1 and 2) than $f_e$. The ratio of $f_e$ to $\sigma^{e}_{ij}$ depends on the value of tradeoff parameter $\lambda$ in Eq. (12). When a large value is used for $\lambda$, there is less weight on $|\boldsymbol{K}_{st}\boldsymbol{f} - \boldsymbol{b}_{st}|_2$ in Eq. (12), and thus $f_e/\sigma^{e}_{ij}$ decreases. Conversely, when a small value is used for $\lambda$, there is more weight on $|\boldsymbol{K}_{st}\boldsymbol{f} - \boldsymbol{b}_{st}|_2$, and thus $f_e/\sigma^{e}_{ij}$ increases. Since $|\boldsymbol{K}_{eq}\boldsymbol{f}|_2$ and $|\boldsymbol{K}_{st}\boldsymbol{f} - \boldsymbol{b}_{st}|_2$ are almost equally weighted in our paper with a selected value of $\lambda = 1$, it is reasonable that there is no significant difference between the values of $f_e$ and $\sigma^{e}_{ij}$ in each simulation in Figs. 5 and 9.

### F. Missing particle stress tensors

The second type of error we investigate is that of missing particle stress tensors. To investigate the influence of this error on inferred forces, we randomly select particles using a random number generator in MATLAB and delete the corresponding rows of $\boldsymbol{K}_{st}$ and $\boldsymbol{b}_{st}$ after all such particles have been identified. If the particle to be deleted has index $p$, we therefore mark rows $6p - 5$ through $6p$ for deletion (for 3D systems). Forces are then inferred using the minimization procedure in Sec. II A without the introduction of any further errors.

Figure 10 illustrates the average normalized inferred force magnitude error as a percentage ($f_e \times 100\%$) and the average orientation error ($\theta_e$), both as functions of the normalized number of missing particles, $n_p = N^{p}_{missing}/N_p$. Both the magnitude and orientation errors remain very close to zero until approximately $n_p = 0.4$. This reflects the fact that the number of unknown force vector components after removal of randomly selected particles, $3N_c$, remains less than the number of equations $6 \times (N_p - N^{p}_{missing})$ until about $n_p \approx 0.4$. When $n_p > 0.4$, there are more unknown force vector components than equations, and both the magnitude and orientation errors begin to increase with $n_p$ as the minimization in Eq. (12) becomes increasingly underconstrained. Nevertheless, errors remain small until $n_p$ exceeds about 0.7, at which point they exceed those obtained in the case of stress tensors with measurement errors in Sec. III E for almost all simulations.

Figure 11 illustrates the average normalized error in inferred particle stresses as a percentage ($\sigma^{e}_{ij} \times 100\%$) and as a function of $n_p$ for the 0.1-MPa uniaxial compression simulation. Figure 11(a) shows ($\sigma^{e}_{ij} \times 100\%$) calculated for all particles in the simulation. Figure 11(b) shows ($\sigma^{e}_{ij} \times 100\%$) calculated only for the particles for which stresses are not supplied to the force inference procedure. Figure 12 illustrates the same errors but for the 0.1-MPa triaxial compression simulation. We note that there is very little influence of applied stress on these results; we therefore plot only the results for 0.1-MPa simulations for brevity. In both the uniaxial and triaxial compression cases, the errors are only present when $n_p > 0.6$ and are not significant until $n_p > 0.8$ for the uniaxial compression case. Remarkably, in both the uniaxial and triaxial cases, stress tensors themselves can be inferred accurately by first inferring forces and then calculating all particle stresses by $\boldsymbol{K}_{st}\boldsymbol{f}$. This suggests that in experiments in which 3DXRD measurements do not yield reliable stress tensors in up to 50% of the particles (e.g. [31]) such stress tensors can be recovered. We conclude that missing particle stress tensors of an experimentally reasonable number (e.g., $n_p < 0.5$ as in [31]) leads to minimal error in both contact force magnitudes and directions.

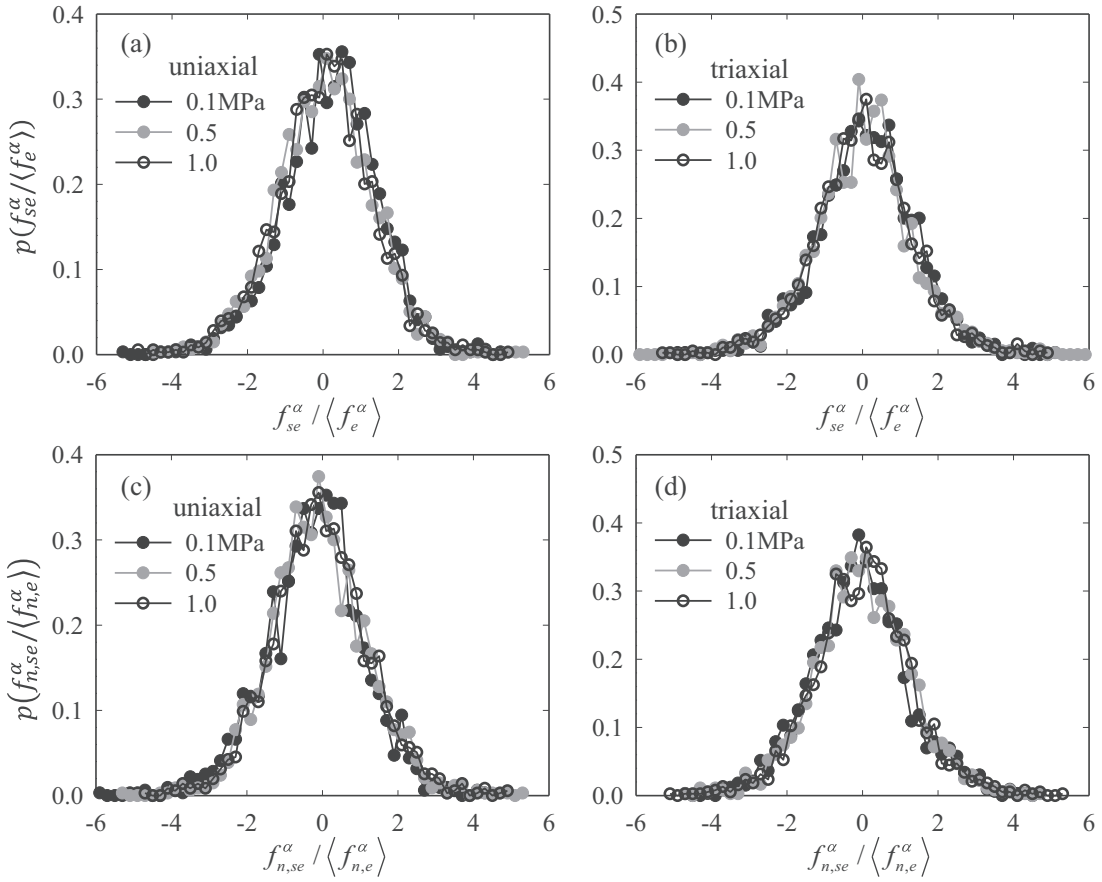


FIG. 7. Probability densities of signed normalized inferred force magnitude errors, $f^{\alpha}_{se}/\langle f^{\alpha}_{e}\rangle$, for (a) uniaxial and (b) triaxial DEM simulations, and signed normalized inferred normal force magnitude errors, $f^{\alpha}_{n,se}/\langle f^{\alpha}_{n,e}\rangle$, for (c) uniaxial and (d) triaxial DEM simulations. In all cases, probability densities follow the normal or Gaussian with mean zero and standard deviation of approximately 1.2.

### G. Missing contact locations

The third type of error we investigate is that of missing contacts. To investigate the influence of this error on inferred forces, we randomly select contacts using a random number generator in MATLAB and delete the corresponding columns of $\boldsymbol{K}_{\mathrm{eq}}$ and $\boldsymbol{K}_{\mathrm{st}}$, and the corresponding rows of $\boldsymbol{f}$, after all such contacts are identified. If the contact to be deleted has index $\alpha$, we therefore mark columns $3\alpha-2$ through $3\alpha$ for deletion in $\boldsymbol{K}_{\mathrm{eq}}$ and $\boldsymbol{K}_{\mathrm{st}}$ (in 3D materials). Forces are then inferred using the minimization procedure in Sec. II A without the introduction of any further errors. We note that in experiments we do not know which contact points may be missing from our analysis. We may miss contacts due to a combination of experimental resolution limits and algorithmic issues, as described in Sec. III A and [36,37].

Figure 13 illustrates the average normalized inferred force magnitude error as a percentage ($f_e \times 100\%$) and the average orientation error ($\theta_e$), both as functions of the normalized number of missing contact points, $n_c = N^c_{\mathrm{missing}}/N_c$. Note that in calculating $f_e$ and $\theta_e$ the denominator in Eqs. (22) and (24) is taken to be $N_c - N^c_{\mathrm{missing}}$ and the sum in the numerators is only over the remaining contacts the rows of which were not deleted. Both $f_e$ and $\theta_e$ increase with $n_c$, although they remain smaller than errors stemming from noise in stress tensors for 0.1-MPa simulations (see Sec. III E) up to about $n_c \approx 0.1$. The force inference procedure is clearly more sensitive to missing contacts than missing stresses. This is not surprising: when a particle's stress is missing, there is less information for the force inference procedure but the ground-truth forces are still a valid minimizing set of forces for Eq. (12). On the other hand, when a particle's contacts are missing, the ground-truth forces may not be a minimizing set of forces for Eq. (12), as can be easily understood if one of two contacts for a diametrically compressed particle is missing.

Although our analysis in this subsection suggests that increasing $n_c$ leads to significantly larger values of $f_e$ and $\theta_e$ than increasing $n_p$, the normalized number of missing contacts, $n_c$, in most high-quality data sets in our prior work (e.g., [5,19,22]) is likely less than 0.01. In such cases, $f_e$ and $\theta_e$ remain close to zero, as shown in Fig. 13.

### H. Contact overdetection

The fourth type of error we investigate is that of contact overdetection. To investigate the influence of this error on inferred forces, we assume the presence of additional contact points between particles, which we call virtual contact points (VCP), when the distance between particle centers minus the sum of their radii is less than an arbitrary threshold, or

$$\frac{|\boldsymbol{c}^p - \boldsymbol{c}^q|_2 - (R_p + R_q)}{R_p + R_q} < \frac{n_r}{100}, \tag{26}$$

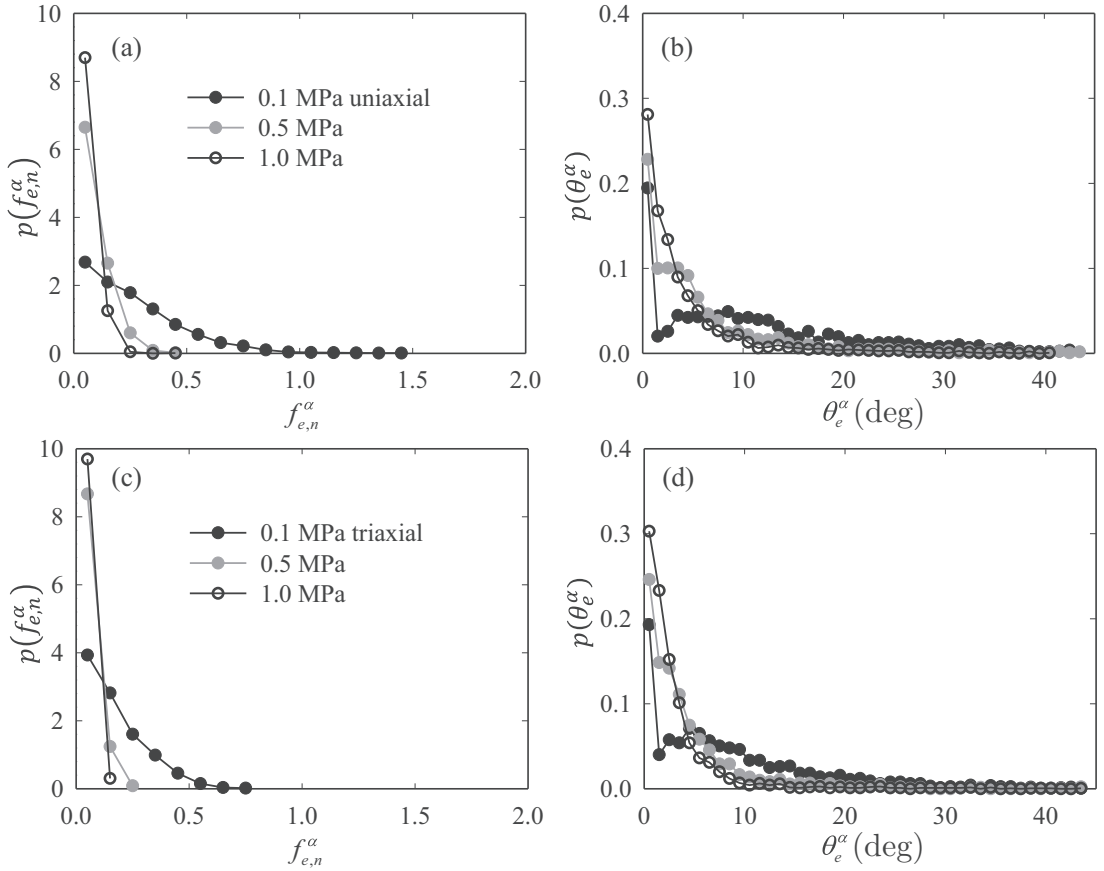


FIG. 8. Probability densities of normalized inferred force magnitude errors ($f^{\alpha}_{e,n}$) and orientation errors ($\theta^{\alpha}_{e}$) for the case when noise is introduced in the particle stress tensors as described in Sec. III E: (a), (b) uniaxial DEM simulations and (c), (d) triaxial DEM simulations.

where $R_p$ and $R_q$ are the radii of particles $p$ and $q$, and $n_r$ is referred to as the normalized resolution. When $n_r > 0$, particles $p$ and $q$ are not in contact. When $n_r = 100$, particles $p$ and $q$ are separated by the sum of their radii. We set $n_r$ to be 0.01, 0.1, 1, 5, 10, and 20, and examine the resulting number of overdetected contacts, $N_{\mathrm{VCP}}$, and the average normalized inferred force magnitude error ($f_e \times 100\%$) and the average orientation error ($\theta_e$) in the 0.1-MPa uniaxial DEM simulation. Table VI provides the results of this analysis, illustrating that both $f_e$ and $\theta_e$ remain very small for all values of $N_{\mathrm{VCP}}$. We conclude that overdetection of contacts alone leads to minimal error in both contact force magnitudes and directions.

TABLE VI. Force magnitude and orientation errors for cases of contact overdetection in the 0.1-MPa uniaxial DEM simulation.

| $n_r$ | $N_{\mathrm{VCP}}$ | $f_e \times 100\%$ | $\theta_e$ |
|---|---|---|---|
| 0.01 | 8 | 0.001 | 0.047 |
| 0.1 | 39 | 0.002 | 0.055 |
| 1 | 166 | 0.002 | 0.065 |
| 5 | 436 | 0.002 | 0.074 |
| 10 | 649 | 0.005 | 0.098 |
| 20 | 994 | 0.005 | 0.099 |

### I. Errors in particle stiffness

The fifth type of error we investigate includes errors in the particle stiffness. As noted in Sec. III A, such errors arise primarily in 2D experiments due to limitations in material characterization. To investigate the effect of this source of error, we scale the ground-truth stress of all particles in the uniaxial and triaxial DEM simulations by an "uncertainty factor," $u_f$, to emulate a scaling of stress due to over- or underestimate of Young's modulus, $E$. We then infer forces using the method of Sec. II A, both in the absence and in the presence of additional errors in the average particle stress tensors.

Figure 14 shows the average normalized inferred force magnitude errors as a percentage and the average inferred force orientation errors as a function of $u_f$. In the absence of additional errors in average particle stress tensors, Figs. 14(a) and 14(b) show that $f_e$ is negligible at $u_f = 1$ and $\theta_e$ is negligible for all values of $u_f$. This latter finding suggests that forces are primarily scaled in magnitude but not direction by changes in $u_f$ (and therefore $E$) between 0 and 4. $f_e$ increases linearly in $u_f$ for $u_f \neq 1$, approaching 100% error as $u_f$ approaches 0 or 2. This again suggests that errors in inferred forces scale linearly with uncertainties in material stiffness in 2D experiments. In the presence of additional noise in particle stress tensors with the magnitude used in Sec. III E, Figs. 14(c) and

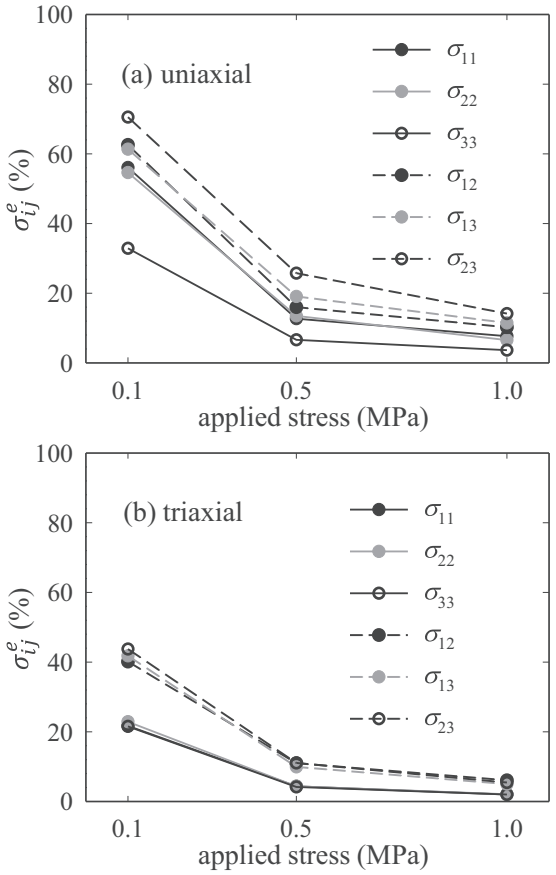


FIG. 9. Average normalized errors in inferred particle stresses, $\sigma_{ij}^e \times 100\%$, for (a) uniaxial DEM simulations and (b) uniaxial DEM simulations for all particles.

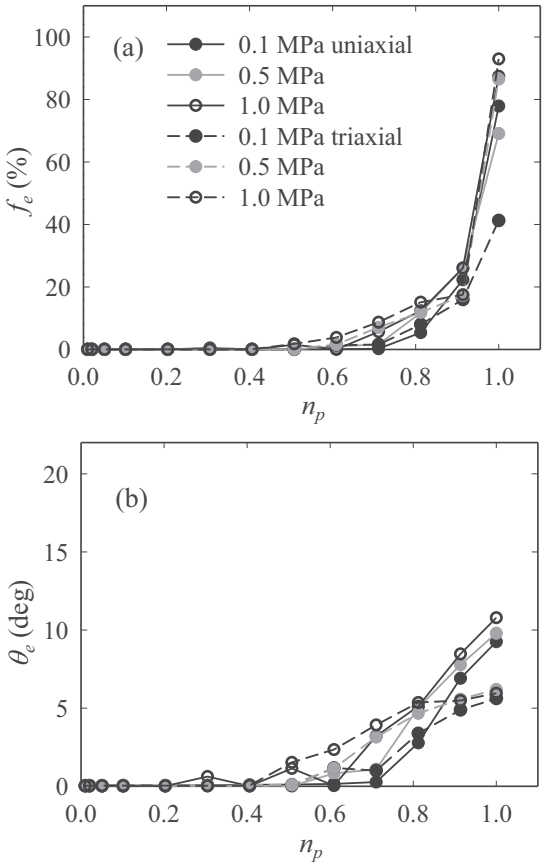


FIG. 10. (a) Average normalized inferred force magnitude error as a percentage ($f_e \times 100\%$) and (b) average inferred force orientation error ($\theta_e$) as a function of normalized number of missing particle stress tensors, $n_p$, as described in Sec. III F.

14(d) show that $f_e$ and $\theta_e$ retain their values from Fig. 5 when $u_f = 1$, as expected. $f_e$ scales approximately linearly with $u_f$, while $\theta_e$ decreases with increasing $u_f$. We conclude that if particle stiffness is known to several percent accuracy or better there will be only several percent error in both contact force magnitudes and directions in addition to any errors induced by noise in stress tensors.

### J. Errors in coefficients of friction

The sixth and final type of error we investigate includes errors in interparticle and particle-boundary friction coefficients. As noted in Sec. III A, interparticle and particle-boundary friction coefficients are often not known with certainty because of the heavily influential effects of roughness and humidity. To investigate the effect of this source of error, we simply modify the coefficient of friction, $\mu$, we use for all contacts in solving Sec. II A. Specifically, we modify $\mu$ of particle-particle contacts, the exact value of which in DEM simulations is 0.4 (Table III). We then infer forces using the method of Sec. II A, both in the absence and in the presence of additional errors in the average particle stress tensors.

Figure 15 shows the average normalized inferred force magnitude errors as a percentage and the average inferred force orientation errors as a function of $\mu$. In the absence of additional errors in average particle stress tensors, Figs. 15(a) and 15(b) show that $f_e$ and $\theta_e$ are negligible when the $\mu$ used in force inference is equal to or greater than its true experimental value. This reflects the fact that both the equilibrium and stress-force relations in Eq. (12) can be satisfied exactly when the coefficient of friction used in the constraint is equal to or greater than its true experimental value. In contrast, when the coefficient of friction used in Eq. (12) decreases to zero, $f_e$ and $\theta_e$ each increase up to approximately 8–11% and 8°–13°, respectively.

In the presence of additional noise in particle stress tensors with the magnitude used in Sec. III E, Figs. 15(c) and 15(d) show that $f_e$ and $\theta_e$ retain their values from Fig. 5 when $\mu$ retains its true value, 0.4, as expected. $f_e$ and $\theta_e$ vary to a small degree when the coefficient of friction varies between 0.0 and 1.0. We note that $f_e$ and $\theta_e$ do not vary significantly from their nominal values obtained in the presence of only errors in particle stress tensors and shown in Fig. 5. This suggests that the coefficient of friction has a secondary role on the accuracy of inferred force magnitudes and orientations.

### K. Analysis of other mixed errors

In the previous subsections, the effects of a single error or of two errors (in the case of Secs. III I and III J) on inferred

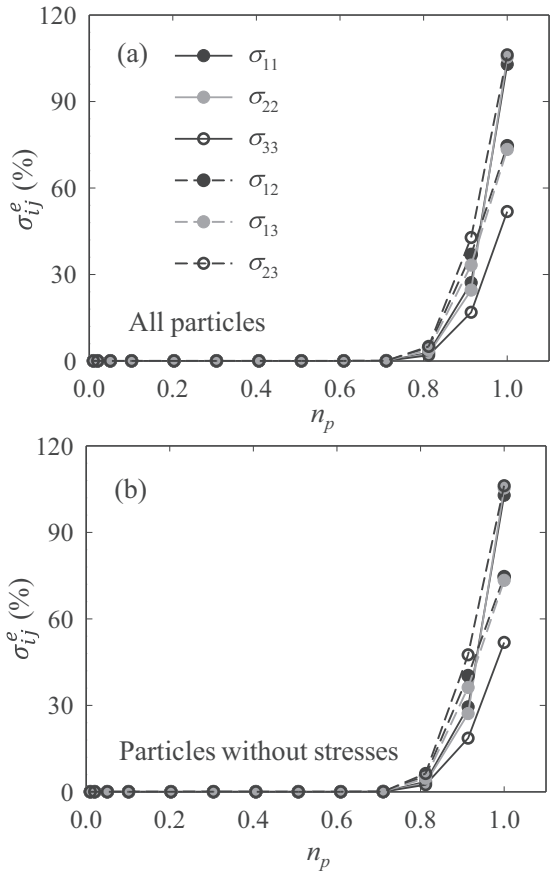


FIG. 11. Average normalized errors in inferred particle stresses, $\sigma_{ij}^e \times 100\%$, for the 0.1-MPa uniaxial DEM simulations for (a) all particles and (b) only particles for which stresses are not supplied to the force inference procedure.

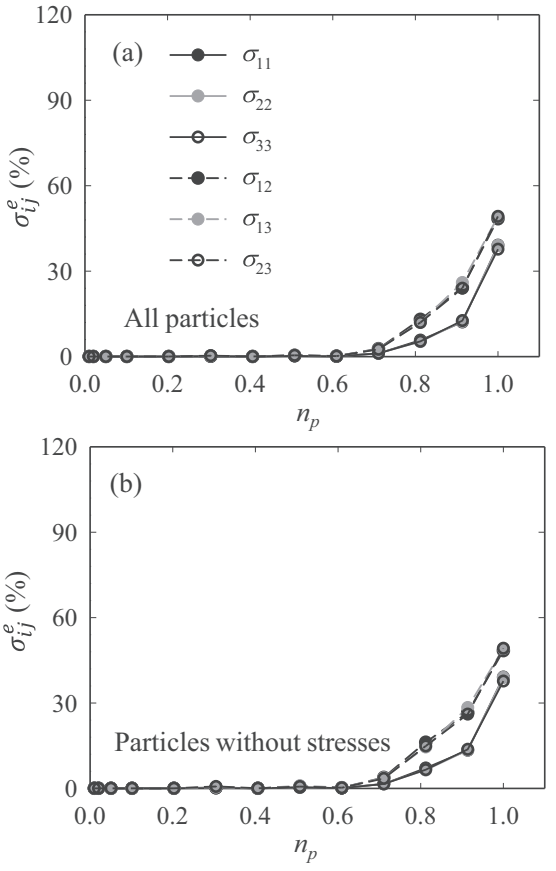


FIG. 12. Average normalized errors in inferred particle stresses, $\sigma_{ij}^e \times 100\%$, for the 0.1-MPa triaxial DEM simulations for (a) all particles and (b) only particles for which stresses are not supplied to the force inference procedure.

force magnitudes and orientations were investigated. Further analysis of mixed errors is provided in Appendix C.

## IV. APPLICATION TO 3D EXPERIMENTAL DATA

In this subsection, we use the experimental data from [22], obtained during uniaxial (T1) and hydrostatic (T2) compression of approximately 900 ruby spheres of diameter 140–150 $\mu$m, to infer interparticle forces and evaluate errors in these forces without ground-truth data. We note that the data from [22] were obtained using *in situ* 3DXRD and XRCT measurements that yielded per-particle stress tensors, particle volumes, and contact locations. Other quantities needed in solving Eq. (12), such as particle stiffness, interparticle friction, and the weight factor $\kappa^p$ were obtained from the literature or calculated using the method in Appendix A. The experiments involved global uniaxial and hydrostatic compression of samples with macroscopic stress levels close to or even below the noise level of an individual particle's stress tensor. More details regarding these experiments and force inference for these experiments using an older method (from [17]) are provided in [22].

### A. Comparison of inferred forces

We first compare the inferred forces from [22] with those obtained with the modified force inference technique of Sec. II A. Figure 16 shows the sum of inferred forces against the top boundary at each load step of each experiment using method 2 with $\lambda = 1$ from Table I, which was used in [22], and using method 3 with $\lambda = 1$ and $j = 2$ from Table I, which was developed in Sec. II A. We observe very similar trends and quantitative values for the sum of inferred forces against the top boundary in both cases. We note, however, that method 3 from Table I provides more robust results in the presence of unit changes or changes in the assumed origin of the coordinate system, as emphasized by analysis in Appendix B. Insets to Fig. 16 show the T1 and T2 sample geometries and the locations at which inferred forces are compared (highlighted with a dark ring).

### B. Estimating errors without ground-truth data

In this subsection, we estimate errors in inferred forces without ground-truth data in two ways. The purpose of this calculation is to provide an example of how errors in inferred forces may be inferred without ground-truth data in future studies. We restrict our analysis to considering only errors in inferred forces due to noise in particle stress tensors—the

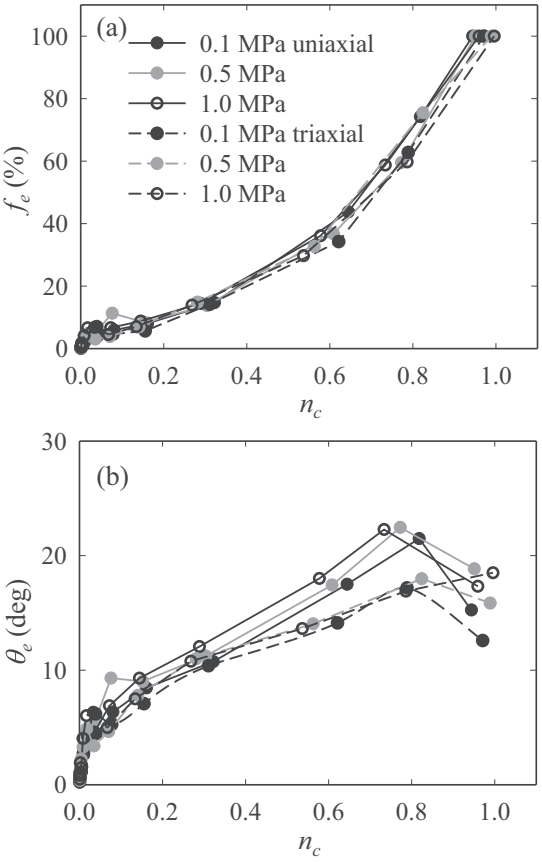


FIG. 13. (a) Average normalized inferred force magnitude error as a percentage ($f_e \times 100\%$) and (b) average inferred force orientation error ($\theta_e$) as a function of normalized number of missing particle contact points, $n_c$.

first row of Table II and the most consistently present error in experiments. The other sources of error are expected to be negligible in these experiments due to the high quality and resolution of 3DXRD and XRCT data.

The first way in which we estimate $f_e$ and $\theta_e$ is by using multivariable regression with the data from Sec. III E, expanded to include simulations in which the particle Young's modulus is varied to be 1, 10, 100, and 500 GPa and in which the applied stress is varied to be 0.1, 0.5, 1, 10, and 50 MPa. These conditions completely span those observed in experiments in [22], permitting us to perform regression with our results to estimate $f_e$ and $\theta_e$. We use results from all simulations to develop regression equations for $f_e$ and $\theta_e$ that are functions of nondimensionless error, $A$, where

$$A = \frac{\Sigma}{|\langle \mathrm{tr}(\bar{\sigma}^p)\rangle|}, \tag{27}$$

the ratio of the standard deviation of on-diagonal stress tensor errors ($\Sigma \approx E \times 10^{-4}$) to the absolute value of the average trace of all particle stress tensors, $|\langle \mathrm{tr}(\bar{\sigma}^p)\rangle|$. Because ruby is a trigonal crystal, the average value of on-diagonal components of the stiffness tensor, $(\mathbb{C}_{11} + \mathbb{C}_{11} + \mathbb{C}_{33})/3$, is used as $E$. As $\mathbb{C}_{11}$ (496.8 GPa) and $\mathbb{C}_{33}$ (498.1 GPa) are almost the same [41], this anisotropy is negligible. Variance of $f_e$ and $\theta_e$ with respect to other variables, such as coordination number $n$, is at least an order of magnitude less significant than variance with respect to $A$ for the range of Young's moduli and applied stress in our simulations. From least-squares regression, we obtain a regression equation for $f_e$ as

$$f_e^{\mathrm{est}} = 0.16A \tag{28}$$

and a regression equation for $\theta_e$ as

$$\theta_e^{\mathrm{est}} = 15.13 - \frac{4.61}{(A + 0.35)}. \tag{29}$$

Figure 17 illustrates the regression results and the data used for regression, showing a very good fit for $A \leqslant 10$.

The second way in which we estimate $f_e$ and $\theta_e$ is by directly using experimental data. In this approach, we first infer forces using Eq. (12) and experimental data; we assume these to be the ground-truth forces. Next, we add noise to on-diagonal and off-diagonal stress tensor components of each particle by drawing them from Gaussian distributions with zero mean and standard deviations of $E \times 10^{-4}$ and $E \times 5 \times 10^{-5}$, respectively. We then infer forces using Eq. (12) and this "noisy" stress data to obtain $f_e^{\mathrm{est}}$ and $\theta_e^{\mathrm{est}}$ for each load step of each experiment with Eq. (22). This approach exploits the fact that stress errors and signed inferred force magnitude errors, $f_{se}^{\alpha}$, have mean zero, as shown in Fig. 7.

The value of $A$ used in regression for experiments T1 and T2, and a comparison of the two approaches for estimating $f_e$ and $\theta_e$ for these experiments, are shown in Fig. 18. This figure shows that the two methods of estimating $f_e$ and $\theta_e$, using regression and using experimental data with added noise, provide similar trends.

Figure 18 also shows $f_e$ and $\theta_e$ for the strong force networks ($f^{\alpha} > \langle f^{\alpha}\rangle$ and $f^{\alpha} > 2\langle f^{\alpha}\rangle$) for experiments T1 and T2. Because absolute values of $f_e$ are constant regardless of the magnitude of specific contact forces (Fig. 6) and $\langle f_{\mathrm{GT}}^{\alpha}\rangle$ that is the denominator of $f_e$ [Eq. (22)] is approximately doubled in the strong force network, $f_e$ in the strong force networks is reduced to half of $f_e$ in the overall force network in Figs. 18(b) and 18(e). Similarly, because $\theta_e$ decreases as the magnitude of contact forces increases (Fig. 6), $\theta_e$ in the strong force network is slightly less than $\theta_e$ in the overall force network in Figs. 18(c) and 18(f).

### C. Missing particle stress tensors

In experiments T1 and T2, stress tensors of approximately 5% of particles were not detected [22]. The presence of missing stress tensors is the second-largest error source among error sources introduced in Table II in these experiments. However, in the mixed analysis in Appendix C, compared with the case when there is only noise in the stress tensor components, the values of $f_e$ (25.6%) and $\theta_e$ (11.1°) change negligibly in the case of both noisy stress tensors and 5% missing stress tensors (to 27.5% and 11.0°, respectively, as shown in Tables VII and XI). Therefore, in this section, we assume that there are no particles missing stress tensors when we infer interparticle forces.

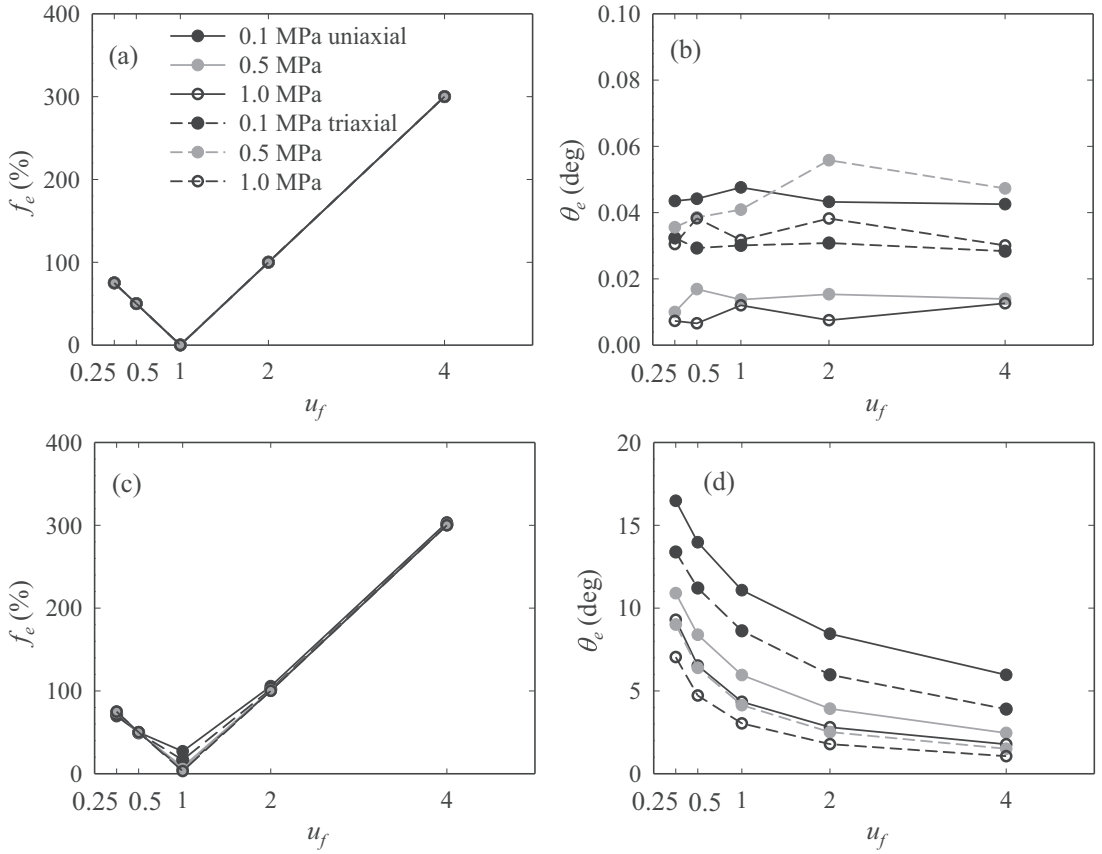


FIG. 14. Effect of stiffness uncertainty, $u_f$, on (a), (c) the average normalized inferred force magnitude errors ($f_e \times 100\%$) and (b), (d) average inferred force orientation errors ($\theta_e$) (c), (d) with and (a), (b) without additional noise added to the particle stress tensors.

### D. Recommendations for experiment design

In experiments T1 and T2, there is a significant error in inferred force magnitude (greater than 40%) (Fig. 18). If only the strong force network is considered ($f^\alpha > \langle f^\alpha \rangle$), $f_e$ is equal to or greater than 20%. In this subsection, we use the findings of this paper to make recommendations that will significantly reduce $f_e$ and $\theta_e$ in future experiments. More accurate inferred force magnitudes and directions will permit

TABLE VII. Average normalized inferred force magnitude errors, $f_e(\%)$, and average inferred force orientation errors, $\theta(^\circ)$, for 0.1-MPa uniaxial simulation. A unit change corresponds to a change from the use of meters to micrometers in all balance laws. An origin change corresponds to a shift in the origin of $(-1, -1, -1)$ km. Noise in the stress tensors with the magnitude used in Sec. III E is denoted (N). The case of missing stresses ($n_p = 0.5$) is denoted (S). The case of missing contacts ($n_c = 0.01$) is denoted (C). The presence of virtual contact points ($n_r = 1$) is denoted (V).

| Method | λ | Change | $j$ | $f_e$ (no error) | $\theta_e$ (no error) | $f_e$ (N) | $\theta_e$ (N) | $f_e$ (S) | $\theta_e$ (S) | $f_e$ (C) | $\theta_e$ (C) | $f_e$ (V) | $\theta_e$ (V) |
|---|---|---|---|---|---|---|---|---|---|---|---|---|---|
| 1 | | None | | 0.0 | 0.0 | 19.4 | 7.9 | 0.0 | 0.0 | 16.9 | 7.4 | 0.0 | 0.1 |
| 1 | | Unit | | 0.0 | 0.0 | 100.1 | 7.8 | 0.0 | 0.1 | 100.0 | 12.6 | 0.0 | 0.1 |
| 1 | | Origin | | 42.3 | 11.0 | 42.8 | 11.0 | 42.1 | 11.0 | 43.5 | 11.5 | 47.3 | 11.8 |
| 2 | 0.1 | None | | 0.0 | 0.1 | 31.1 | 14.6 | 0.3 | 0.4 | 6.7 | 5.1 | 0.0 | 0.1 |
| 2 | 0.1 | Unit | | 0.0 | 0.1 | 38.2 | 15.2 | 0.4 | 0.5 | 8.4 | 6.6 | 0.0 | 0.1 |
| 2 | 0.1 | Origin | | 0.5 | 1.1 | 38.7 | 16.3 | 9.6 | 6.7 | 7.7 | 6.8 | 1.0 | 1.9 |
| 2 | 1.0 | None | | 0.0 | 0.0 | 22.4 | 10.0 | 0.1 | 0.3 | 8.1 | 5.1 | 0.0 | 0.1 |
| 2 | 1.0 | Unit | | 0.0 | 0.1 | 31.3 | 13.3 | 0.0 | 0.1 | 8.3 | 6.0 | 0.0 | 0.1 |
| 2 | 1.0 | Origin | | 0.2 | 0.5 | 33.4 | 13.9 | 7.2 | 5.3 | 7.8 | 6.3 | 1.2 | 2.1 |
| 2 | 10.0 | None | | 0.0 | 0.0 | 18.4 | 8.0 | 0.1 | 0.2 | 16.0 | 7.3 | 0.0 | 0.1 |
| 2 | 10.0 | Unit | | 0.0 | 0.1 | 38.7 | 10.9 | 0.0 | 0.1 | 8.6 | 6.1 | 0.0 | 0.1 |
| 2 | 10.0 | Origin | | 29.0 | 10.0 | 33.1 | 13.8 | 35.7 | 10.5 | 31.1 | 10.4 | 35.5 | 11.0 |
| 3 | 1.0 | | 1 | 0.0 | 0.1 | 35.3 | 13.9 | 0.0 | 0.0 | 0.2 | 0.1 | 0.0 | 0.1 |
| 3 | 1.0 | | 2 | 0.0 | 0.0 | 25.6 | 11.1 | 0.0 | 0.1 | 3.0 | 0.1 | 0.0 | 0.1 |

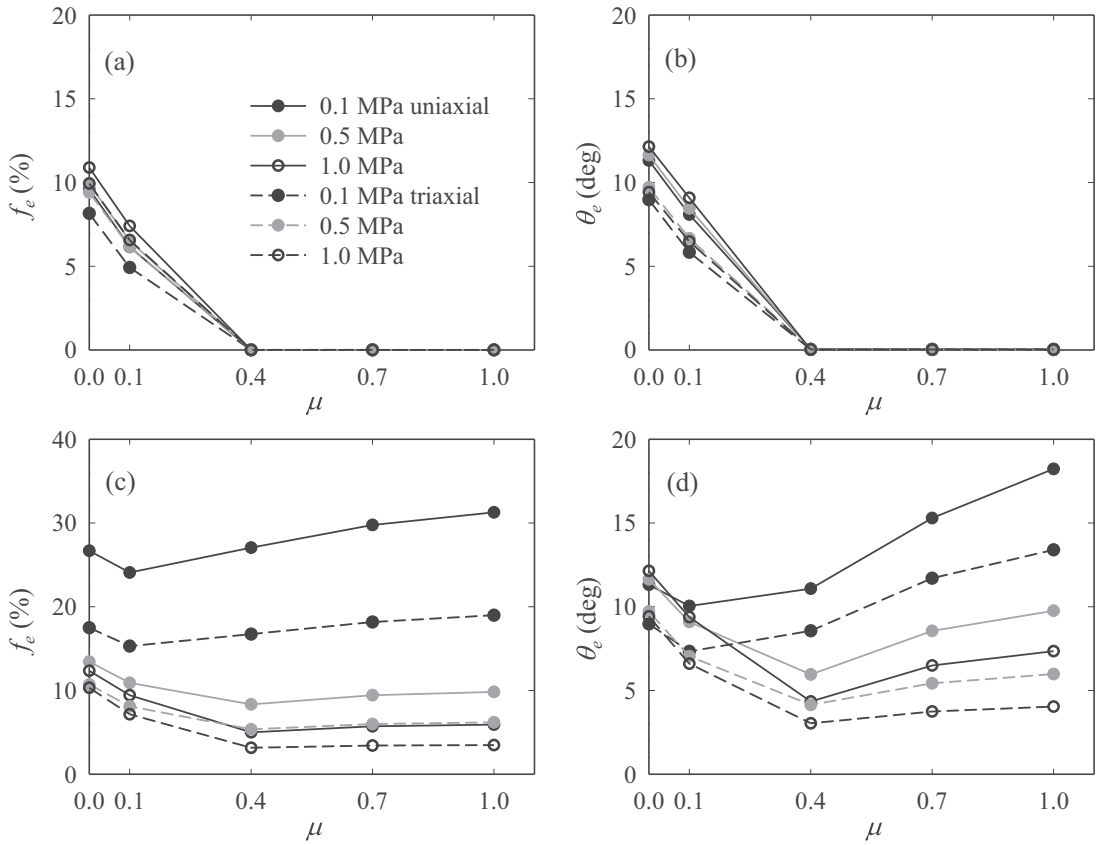


FIG. 15. Effect of friction uncertainty on (a), (c) the average normalized inferred force magnitude errors ($f_e \times 100\%$) and (b), (d) average inferred force orientation errors ($\theta_e$) (c), (d) with and (a), (b) without additional noise added to the particle stress tensors.

experimental studies in which meaningful information can be extracted from the weak force network, which is thought to be important in processes including jamming and force chain buckling [42,43].

We have shown that $f_e$ is linearly proportional to $A$ in Eq. (28) and Fig. 17 for $A < 10$. Assuming materials are approximately linear elastic and approximately isotropic, we can rewrite Eq. (27) as

$$A \approx \frac{E \times (1-2\nu) \times \epsilon^e}{E \times |\langle \mathrm{tr}(\bar{\epsilon}^p)\rangle|} = \frac{(1-2\nu) \times \epsilon^e}{|\langle \mathrm{tr}(\bar{\epsilon}^p)\rangle|}, \tag{30}$$

where $\nu$ is Poisson's ratio, $\epsilon^e$ is the magnitude of noise on a particle's strain tensor (e.g., on the on-diagonal component), and $|\langle \mathrm{tr}(\bar{\epsilon}^p)\rangle|$ is the absolute value of the average trace of all particle strain tensors. We assume that materials are elastic because 3DXRD analysis assumes elasticity [44]. In Eq. (30), we observe that the magnitude of $E$ does not affect the magnitude of $A$. Furthermore, $\epsilon^e$ is fixed by 2D area detector resolution and bit depth, while $|\langle \mathrm{tr}(\bar{\epsilon}^p)\rangle|$ is proportional to the average strain or stress in the bulk granular material. This provides two possible methods for reducing $A$ in a given experiment.

(1) Reduce $\epsilon^e$ by optimizing 2D area detector parameters (increasing bit depth from 8-bit found in many detectors to 16-bit, increasing the number of angular increments at which diffraction images are obtained, and possibly increasing the sample-to-detector distance). With this approach and currently available detectors, we expect that errors in on-diagonal strain tensor components can be driven down to $\epsilon^e = 2\times10^{-5}$, rather than the current value of about $\epsilon^e = 10^{-4}$ (an improvement by a factor of 5, based on discussions with beamline staff at the Advanced Photon Source).

(2) Increase $|\langle \mathrm{tr}(\bar{\epsilon}^p)\rangle|$ by selecting a material that can sustain significant elastic strains prior to plastic deformation or fracture. Particles in our prior experiments with ruby are likely to feature a low elastic strain limit, but other single crystals may be able to sustain higher elastic strains.

It is noteworthy that optimizing area detector parameters to decrease $\epsilon^e$ and increasing $|\langle \mathrm{tr}(\bar{\epsilon}^p)\rangle|$ by appropriate selection of crystals used in experiments operate independently. These methods affect the numerator and denominator in Eq. (30), respectively. By actively seeking both modifications in future experiments, we expect a significant reduction in errors in inferred force magnitude and orientation.

## V. DISCUSSION

In Sec. II A, we modified the force inference technique proposed in [17] to make it insensitive to the choice of units and the coordinate system origin used in analysis. We then performed a systematic analysis of how a subset of the possible experimental errors in Table II leads to errors in inferred forces. Our results and their implications include the following.

(1) Noise in particle stress tensors leads to errors in inferred force magnitudes and directions. These errors in inferred

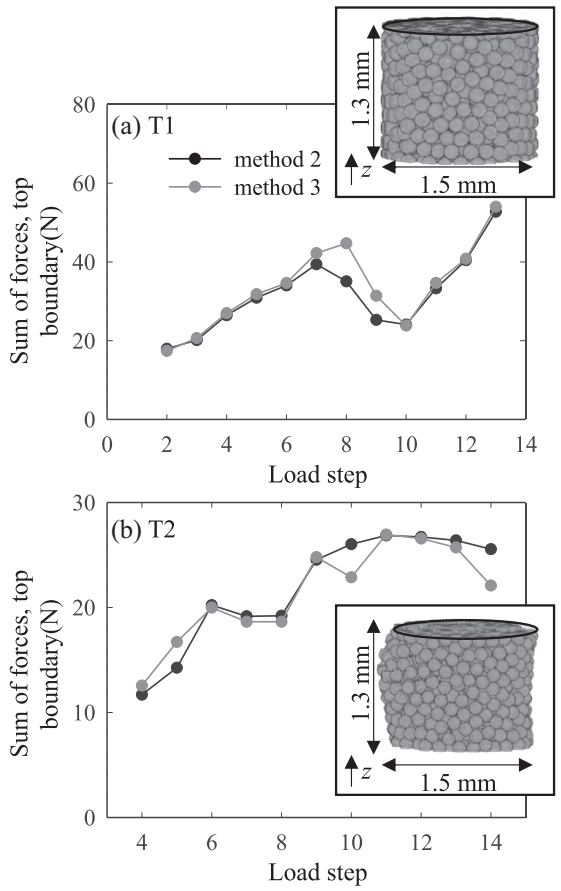


FIG. 16. (a) Sum of inferred forces between particles and the top boundary in experiment T1 using method 2 from Table I (also used in [22]) and using method 3 from Table I. The inset shows the sample with the top boundary circled in black and lightly shaded. (b) Same as (a) but for experiment T2.

forces decay with increasing applied sample stress (Fig. 5) because the magnitude of noise in particle stress is a fixed property of experimental resolution. These errors are uncorrelated with inferred forces at specific contacts (Fig. 6), implying that the largest inferred forces in a granular packing can still be accurately characterized (Fig. 8).

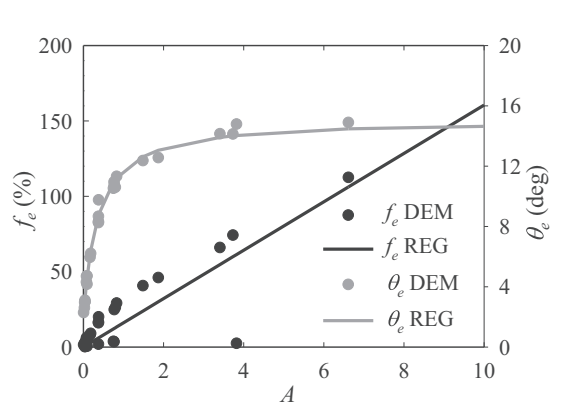


FIG. 17. Regression (REG) curves for $f_e$ and $\theta_e$ using $A$ (described in text). Dots are discrete element method simulation results data for $f_e$ and $\theta_e$.

(2) Missing particle stress tensors alone lead to errors in inferred force magnitudes and directions only when the number of unknown force vector components in a granular material begins to exceed the number of equations (Fig. 10). Stresses calculated using the resulting inferred forces are very accurate for particles for which particle stress tensors were not missing. Stresses calculated using inferred forces are surprisingly accurate also for particles for which particle stress tensors were missing. This latter finding suggests a route to "recovering" stresses missed in a 3DXRD experiment (e.g., a problem in prior work [31]).

(3) Missing contacts and contact overdetection lead to small errors in inferred force magnitudes and orientations for values of $n_c$ and $N_{\mathrm{VCP}}$ expected to be found in experiments—less than 5% and a few contacts, respectively—as shown in Fig. 13 and Table VI.

(4) Errors in Young's modulus and interparticle friction lead to small errors in inferred force magnitudes and orientations when they are within a few percent of their actual values (Figs. 14 and 15).

(5) Because there is no ground truth for inferred forces in experimental data, we presented two methods of estimating error in inferred forces magnitude obtained in experiments: (i) using a regression curve obtained from DEM results which indicated that $f_e$ is linearly proportional to a nondimensional measure of error, $A$, over a broad range of Young's moduli and sample stresses, and (ii) applying noise on experimentally measured stress tensors, which were assumed to be ground truth. In method (ii), because $f^\alpha_{se}/\langle f^\alpha_e\rangle$ follows a normal distribution with a mean of zero (Fig. 7), the estimated value of $\langle f^\alpha\rangle$ by using method (ii) and the true value of $\langle f^\alpha\rangle$ would be almost the same. Therefore, we deduce that $f_e$ obtained from method (ii) is almost the same with $f_e$ obtained using the true value of $\langle f^\alpha\rangle$ in the denominator. Similarly, in method (i), $|\langle \mathrm{tr}(\bar{\sigma}^p)\rangle|$ in the denominator in $A$ [Eq. (27)] of experimental data would be almost the same as that of the true values since stress errors follow a normal distribution with a mean of zero. Even though the two methods have different assumptions, their predictions of $f_e$ and $\theta_e$ match well for $A < 10$.

(6) We reasoned that $\epsilon^e$, the typical error in a component of the strain tensor obtained from 3DXRD analysis, and $|\langle \mathrm{tr}(\bar{\epsilon}^p)\rangle|$, which reflects a measure bulk sample stress, operate independently in decreasing $A$ and therefore $f_e$. We also reasoned that each of $\epsilon^e$ and $|\langle \mathrm{tr}(\bar{\epsilon}^p)\rangle|$ can be independently modified by optimizing area detector parameters and selecting crystals with a large elastic strain limit. We therefore proposed both modifications in future experiments to obtain significantly lower errors on inferred force magnitudes (perhaps by a factor of 5) and on force orientations. Such modifications may enable experiments in which even weak force networks may be accurately obtained.

## VI. CONCLUSION

We have provided a modified version of a force inference technique applicable to 2D and 3D experimental data and a systematic study of how errors in experimental measurements lead to errors in inferred forces. We notably showed that forces greater than the mean are inferred accurately even in the presence of experimental noise in particle stress tensors.

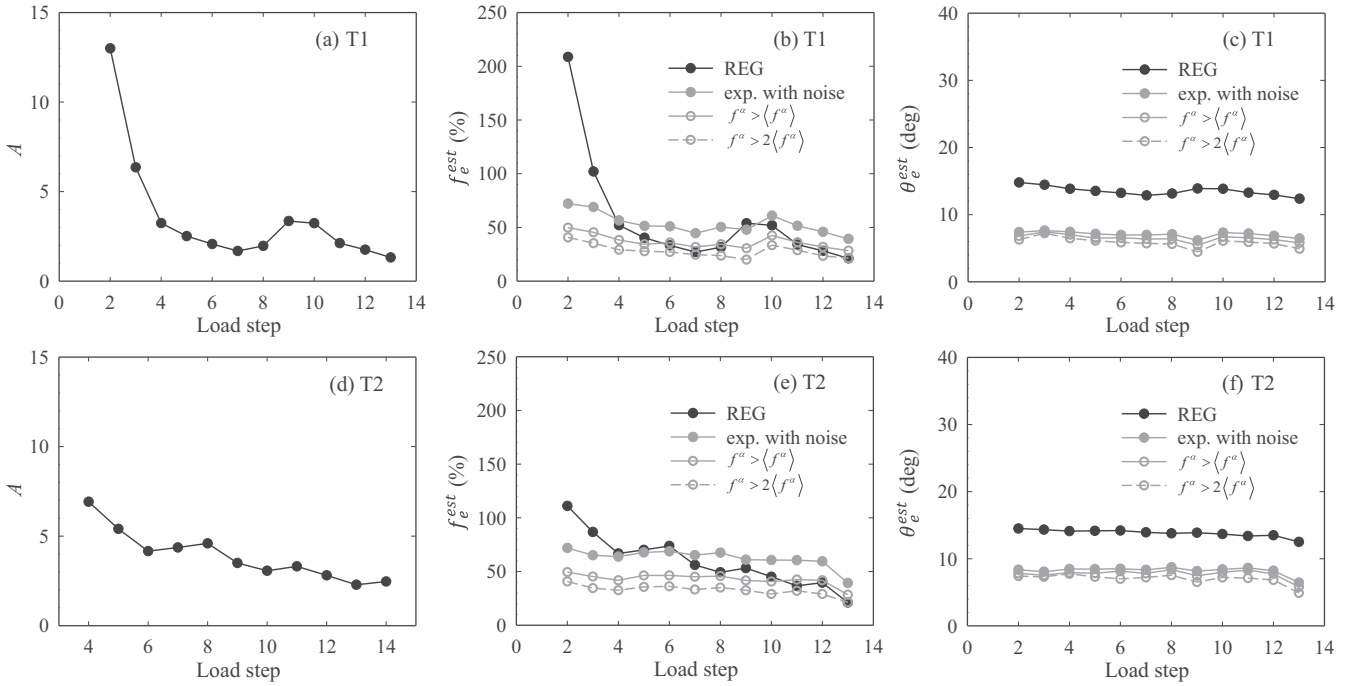


FIG. 18. (a) $A$ from experiment T1. (b) Estimate of $f_e$ using Eq. (28) (labeled REG) and using synthetic noise added to experimental measurements for the overall force network (labeled exp. with noise) and strong networks (labeled $f^\alpha > \langle f^\alpha \rangle$ and $f^\alpha > 2\langle f^\alpha \rangle$) for experiment T1. (c) Estimate of $\theta_e$ using Eq. (29) and using synthetic noise added to experimental measurements for overall and strong force networks for experiment T1. (d) $A$ from experiment T2. (e) The same as (b) but for experiment T2. (f) The same as (c) but for experiment T2.

We also notably showed that stresses can be "recovered" in particles for which experimental stress measurements are absent in cases when the number of missing particle stress tensors approaches 50%. Based on our results, we provided recommendations on area detector optimization and particle selection that will improve force inference accuracy in future experiments. We expect such future experiments to shed light on not only the role of the strong force network, but also on the role of the weak force network in the mechanical behavior and properties of granular packings.


## ACKNOWLEDGMENTS

.This research was supported by the U.S. National Science Foundation CAREER Grant No. CBET-1942096. This support is greatly appreciated. Experimental data comes from synchrotron beamtime at the European Synchrotron Radiation Facility and was obtained under Proposal No. ma-3373. We thank Dr. Jonathan P. Wright, Dr. Marta Majkut, Dr. Jonas Engqvist, Dr. Eric B. Herbold, and Dr. Stephen A. Hall for assistance with these experiments.


## APPENDIX A: DERIVATION OF WEIGHT FACTOR $\kappa^p$

Consider a 2D circular particle $p$ with contacts $i$ and $j$ as shown in Fig. 19. The coordination number, $N$, of particle $p$ is 2. If $\kappa^p = 1$, as in prior versions of the force-inference technique [17], Eqs. (3) and (8), encompassing six equations, can be written

$$\begin{bmatrix} 1 & 0 & 1 & 0 \\ 0 & 1 & 0 & 1 \\ x_2^i & x_1^i & -x_2^j & x_1^j \\ x_1^i & 0 & x_1^j & 0 \\ 0 & x_2^i & 0 & x_2^j \\ x_2^i & x_1^i & x_2^j & x_1^j \end{bmatrix} \begin{bmatrix} f_1^i \\ f_2^i \\ f_1^j \\ f_2^j \end{bmatrix} = \begin{bmatrix} 0 \\ 0 \\ 0 \\ V_p \bar{\sigma}_{11}^p \\ V_p \bar{\sigma}_{22}^p \\ 2V_p \bar{\sigma}_{12}^p \end{bmatrix}. \tag{A1}$$

The first equation in Eq. (A1) requires that

$$f_1^j = -f_1^i, \tag{A2}$$

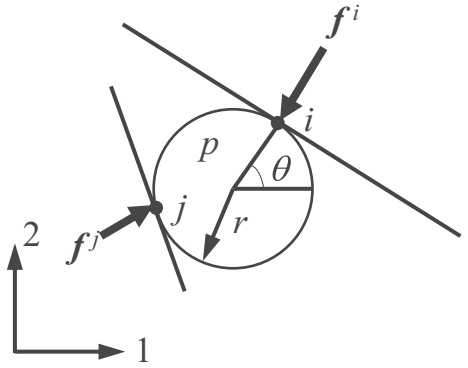


FIG. 19. Illustration of a particle in equilibrium with two contacts.

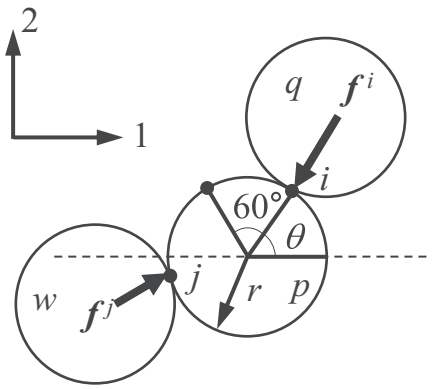


FIG. 20. Illustration of particle $p$ with two contacts at points $i$ and $j$. Particle $p$ is in equilibrium. We consider particle $q$ to remain above the dashed line and particle $w$ to locate either above or below the dashed line.

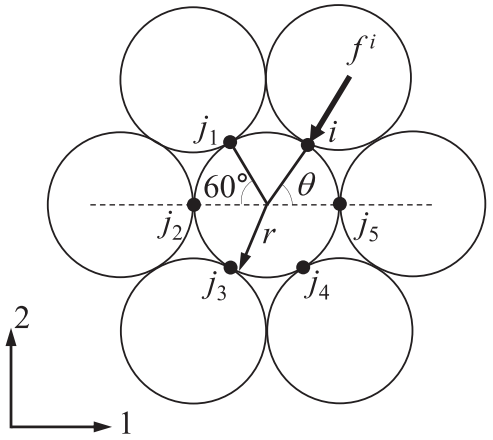


FIG. 21. Illustration of particle $p$ in equilibrium with six contacts with surrounding particles at points $i$, $j_1$, $j_2$, $j_3$, $j_4$, and $j_5$.

or, after substitution of Eq. (A2) back into the first equation,

$$(1-1)f_1^i = 0. \tag{A3}$$

Using the fourth equation in Eq. (A1) with Eq. (A2) gives

$$\left[\left(x_1^i - x_1^j\right) - \left(x_1^i - x_1^j\right)\right]f_1^i = 0. \tag{A4}$$

The similarity of Eqs. (A3) and (A4) illustrates that the stress equations encapsulated in Eq. (A1) can be obtained in this example by multiplying the force balance equations by a factor of $\kappa^p = (x_1^i - x_1^j)$. Multiplying the force balance equations [the first two equations in Eq. (A1)] by $\kappa^p$ also gives them units of length times force, the same units that the moment balance and stress equations have [the last four equations in Eq. (A1)].

Now consider a similar analysis for the case of coordination number, $N$, equal to 3, with a particle $p$ having contacts $i$, $j$, and $k$. The first force balance and first stress balance equations are

$$f_1^i + f_1^j + f_1^k = 0, \tag{A5}$$

$$x_1^i f_1^i + x_1^j f_1^j + x_1^k f_1^k = V_p \bar{\sigma}_{11}^p. \tag{A6}$$

From the first equation,

$$f_1^k = -f_1^i - f_1^j. \tag{A7}$$

Plugging this into Eq. (A6) and rearranging yields

$$\left[\left(x_1^i - x_1^k\right) - \left(x_1^i - x_1^k\right)\right]f_1^i + \left[\left(x_1^j - x_1^k\right) - \left(x_1^j - x_1^k\right)\right]f_1^j = 0. \tag{A8}$$

Rearrangement of Eq. (A5) in a similar manner to the rearrangement performed to obtain Eq. (A3) yields

$$(1-1)f_1^i + (1-1)f_1^j = 0. \tag{A9}$$

Comparison of Eqs. (A8) and (A9) reveals that the stress equations for $N = 3$ cannot be obtained simply by multiplying the force balance equations by $(x_1^i - x_1^k)$ or $(x_1^j - x_1^k)$, as was the case for $N = 2$. Rather, some length scale between $x_1^i - x_1^k$ and $x_1^j - x_1^k$ should be used.

Consider Fig. 20 ($N = 2$) and the quantity $x_1^i - x_1^j$. The average value of $x_1^i - x_1^j$ in the range $0 \leqslant \theta \leqslant \pi/2$ ($x_1^i$ remains above the dashed line) is

$$|x_1^i - x_1^j|_{\text{avg}} = \begin{cases} r(2\cos\theta + 1)/2 & \text{if } 0 \leqslant \theta \leqslant 30^\circ \\ r(4\cos\theta + |\cos(\theta + 60^\circ)| + 2)/4 & \text{if } 30^\circ \leqslant \theta \leqslant 90^\circ \end{cases}. \tag{A10}$$

We consider this case to be required for equilibrium without considering Coulomb friction, the value of which would more precisely constrain the relative angles of contacts $i$ and $j$. Integrating from $0^\circ$ to $\pi/2$ yields

$$\kappa^p = \frac{2}{\pi}\int_0^{\pi/2} \left|x_1^i - x_1^j\right|_{\text{avg}} d\theta \approx 1.176r. \tag{A11}$$

Employing this value of $\kappa^p$ in Eq. (6) ensures equal units for all balance laws used in minimization and also eliminates sensitivity to a change of scale (e.g., using millimeters instead of meters in the minimization).

Repeating the procedure for the case of $N = 6$ shown in Fig. 21 yields an average value for the distance between any two contacts of

$$\left|x_1^i - x_1^j\right|_{\text{avg}} = r(|2\cos\theta| + |\cos\theta - \cos(\theta + 60^\circ)| + |\cos\theta + \cos(\theta - 60^\circ)| + |\cos\theta + \cos(\theta + 60^\circ)| + \cos\theta - \cos(\theta - 60^\circ)|)/5. \tag{A12}$$

TABLE VIII. Average normalized inferred force magnitude errors, $f_e(\%)$, and average inferred force orientation errors, $\theta(^\circ)$, for 0.1-MPa triaxial simulation. A unit change corresponds to a change from the use of meters to micrometers in all balance laws. An origin change corresponds to a shift in the origin of $(-1, -1, -1)$ km. Noise in the stress tensors with the magnitude used in Sec. III E is denoted (N). The case of missing stresses ($n_p = 0.5$) is denoted (S). The case of missing contacts ($n_c = 0.01$) is denoted (C). The presence of virtual contact points ($n_r = 1$) is denoted (V).

| Method | λ | Change | $j$ | $f_e$ (no error) | $\theta_e$ (no error) | $f_e$ (N) | $\theta_e$ (N) | $f_e$ (S) | $\theta_e$ (S) | $f_e$ (C) | $\theta_e$ (C) | $f_e$ (V) | $\theta_e$ (V) |
|---|---|---|---|---|---|---|---|---|---|---|---|---|---|
| 1 | | None | | 0.1 | 0.2 | 13.9 | 6.6 | 0.6 | 0.7 | 39.1 | 10.1 | 0.0 | 0.1 |
| 1 | | Unit | | 0.0 | 0.0 | 100.0 | 6.5 | 0.5 | 0.6 | 100.0 | 10.5 | 0.0 | 0.0 |
| 1 | | Origin | | 38.3 | 8.1 | 38.4 | 8.1 | 42.5 | 8.3 | 38.4 | 9.1 | 42.1 | 8.8 |
| 2 | 0.1 | None | | 0.0 | 0.1 | 21.2 | 12.6 | 1.0 | 1.2 | 4.9 | 4.7 | 0.0 | 0.1 |
| 2 | 0.1 | Unit | | 0.0 | 0.1 | 25.9 | 13.9 | 8.4 | 4.9 | 8.6 | 7.6 | 0.0 | 0.1 |
| 2 | 0.1 | Origin | | 1.0 | 1.5 | 26.3 | 13.9 | 8.2 | 5.5 | 8.0 | 6.2 | 1.2 | 1.9 |
| 2 | 1.0 | None | | 0.0 | 0.0 | 14.7 | 7.6 | 0.5 | 0.6 | 5.8 | 4.5 | 0.0 | 0.1 |
| 2 | 1.0 | Unit | | 0.0 | 0.1 | 21.4 | 11.9 | 1.5 | 1.5 | 7.7 | 6.7 | 0.0 | 0.1 |
| 2 | 1.0 | Origin | | 0.2 | 0.5 | 19.9 | 11.0 | 9.6 | 6.0 | 7.1 | 5.8 | 1.5 | 2.1 |
| 2 | 10.0 | None | | 0.0 | 0.0 | 13.6 | 6.5 | 0.5 | 0.6 | 11.7 | 6.3 | 0.0 | 0.0 |
| 2 | 10.0 | Unit | | 0.0 | 0.1 | 21.3 | 11.9 | 0.9 | 1.0 | 8.3 | 6.8 | 0.0 | 0.1 |
| 2 | 10.0 | Origin | | 20.8 | 7.3 | 24.8 | 7.8 | 24.0 | 7.6 | 19.9 | 7.8 | 23.2 | 8.0 |
| 3 | 1.0 | | 1 | 0.0 | 0.0 | 21.5 | 11.1 | 0.0 | 0.0 | 0.2 | 0.1 | 0.0 | 0.0 |
| 3 | 1.0 | | 2 | 0.0 | 0.0 | 16.5 | 8.6 | 0.1 | 0.3 | 0.8 | 1.1 | 0.0 | 0.0 |

TABLE IX. Average normalized inferred force magnitude errors, $f_e(\%)$, and average inferred force orientation errors, $\theta(^\circ)$, for 0.1-MPa uniaxial simulation. Noise in the stress tensors with the magnitude used in Sec. III E is present in all cases. The case of missing stresses ($n_p = 0.5$) is denoted (S1). The case of missing contacts ($n_c = 0.01$) is denoted (C). The presence of virtual contact points ($n_r = 1$) is denoted (V).

| $j$ | $f_e$ (S1) | $\theta_e$ (S1) | $f_e$ (C) | $\theta_e$ (C) | $f_e$ (V) | $\theta_e$ (V) | $f_e$ (S1+C) | $\theta_e$ (S1+C) | $f_e$ (S1+V) | $\theta_e$ (S1+V) | $f_e$ (C+V) | $\theta_e$ (C+V) | $f_e$ (S1+C+V) | $\theta_e$ (S1+C+V) |
|---|---|---|---|---|---|---|---|---|---|---|---|---|---|---|
| 1 | 43.6 | 14.8 | 36.4 | 14.5 | 37.3 | 15.2 | 84.6 | 23.9 | 46.6 | 14.5 | 36.6 | 15.8 | 85.9 | 23.7 |
| 2 | 34.1 | 12.2 | 28.5 | 11.7 | 27.6 | 11.9 | 82.2 | 24.1 | 38.3 | 13.1 | 33.9 | 19.5 | 81.8 | 23.9 |

TABLE X. Average normalized inferred force magnitude errors, $f_e(\%)$, and average inferred force orientation errors, $\theta(^\circ)$, for 0.1-MPa uniaxial simulation. Noise in the stress tensors with the magnitude used in Sec. III E is present in all cases. The case of missing stresses ($n_p = 0.25$) is denoted (S2). The case of missing contacts ($n_c = 0.01$) is denoted (C). The presence of virtual contact points ($n_r = 1$) is denoted (V).

| $j$ | $f_e$ (S2) | $\theta_e$ (S2) | $f_e$ (S2+C) | $\theta_e$ (S2+C) | $f_e$ (S2+V) | $\theta_e$ (S2+V) | $f_e$ (S2+C+V) | $\theta_e$ (S2+C+V) |
|---|---|---|---|---|---|---|---|---|
| 1 | 39.7 | 14.2 | 81.2 | 21.6 | 40.3 | 14.8 | 82.7 | 23.6 |
| 2 | 30.9 | 11.7 | 78.3 | 21.3 | 31.4 | 12.2 | 81.1 | 23.8 |

TABLE XI. Average normalized inferred force magnitude errors, $f_e(\%)$, and average inferred force orientation errors, $\theta(^\circ)$, for 0.1-MPa uniaxial simulation. Noise in the stress tensors with the magnitude used in Sec. III E is present in all cases. The case of missing stresses ($n_p = 0.05$) is denoted (S3). The case of missing contacts ($n_c = 0.01$) is denoted (C). The presence of virtual contact points ($n_r = 1$) is denoted (V).

| $j$ | $f_e$ (S3) | $\theta_e$ (S3) | $f_e$ (S3+C) | $\theta_e$ (S3+C) | $f_e$ (S3+V) | $\theta_e$ (S3+V) | $f_e$ (S3+C+V) | $\theta_e$ (S3+C+V) |
|---|---|---|---|---|---|---|---|---|
| 1 | 36.9 | 15.1 | 79.4 | 19.5 | 37.7 | 15.4 | 74.1 | 18.8 |
| 2 | 27.5 | 11.0 | 68.8 | 18.8 | 28.7 | 11.7 | 69.6 | 18.8 |

Integrating yields

$$\kappa^p = \frac{1}{\pi}\int_0^\pi \left|x_1^i - x_1^j\right|_{\text{avg}} d\theta \approx 0.9504r. \tag{A13}$$

In this analysis, particles are assumed to be of equal radius.

We can perform a similar analysis to obtain $\kappa^p$ for the 3D problem of spheres in contact. We choose to obtain $\kappa^p$ in three dimensions by calculating the upper and lower bounds on $\kappa^p$ for a given coordination number, $N$, and then taking the average of the bounds. For a sphere with two contacts, the upper bound is $\kappa^p \approx 1.176r$, the lower bound is $\kappa^p = 1.137r$ and the average is $\kappa^p = 1.157r$. For a sphere with $N = 12$, analysis of a variety of crystalline packing structures gives the average value of $\kappa^p \approx 0.93r$. An appropriate general method for selecting $\kappa^p$ is

$$\kappa^p = \begin{cases} (-0.0565n + 1.2894)r & \text{for circles,} \\ (-0.02216n + 1.2008)r & \text{for spheres.} \end{cases} \tag{A14}$$

We use Eq. (A14) with $n$ as the average coordination number for a packing of particles for all analysis in the main text of this paper. $\kappa^p$ varies per particle, and thus we can also study a case in which a granular packing features a more significant variation in particle size than the cases we considered here.

## APPENDIX B: COMPARISON OF FORCE INFERENCE METHODS

We employed all of the methods shown in Table I to infer forces for the 0.1-MPa uniaxial and 0.1-MPa triaxial simulations in the presence and absence of errors and for scenarios in which the origin or units are altered. Tables VII and VIII summarize the results of this analysis. A unit change corresponds to a change from the use of meters to micrometers in all balance laws. An origin change corresponds to a shift in the origin of $(-1, -1, -1)$ km. Noise in the stress tensors with the magnitude used in Sec. III E is denoted (N). The case of missing stresses ($n_p = 0.5$) is denoted (S). The case of missing contacts ($n_c = 0.01$) is denoted (C). The presence of virtual contact points ($n_r = 1$) is denoted (V). From Tables VII and VIII, we see that method 3 developed in Sec. II A with the two-norm ($j = 2$) consistently provides comparable or superior results when compared with any of the other methods, with or without changes in units or origin, and with any of the choices of $\lambda$ for method 2.

## APPENDIX C: ANALYSIS OF MIXED ERRORS

In this subsection, we investigate the scenario of the simultaneous presence of multiple errors. In particular, we study the simultaneous effects of errors in particle stress tensors and both missing contacts and contact overdetection. In practice, all three of these errors may be present in a single experiment, depending on parameters of the experiments.

Table IX shows $f_e$ and $\theta_e$ for minimization with Eq. (12) in the presence of 50% missing stress tensors (S1), noise in the remaining stress tensors, 1% missing contacts (C), and the presence of 1% virtual contacts (V). Table X contains the same information as Table IX but for the 25% missing stress tensors (S2). Table XI contains the same information as Table IX but for the 5% missing stress tensors (S3). In all cases in these tables, analysis is performed on the 0.1-MPa uniaxial simulation and noise is introduced in the stress tensors with the magnitude used in Sec. III E.


[1] J. F. Peters, M. Muthuswamy, J. Wibowo, and A. Tordesillas, Characterization of force chains in granular material, Phys. Rev. E **72**, 041307 (2005).

[2] S. D. Walsh, A. Tordesillas, and J. F. Peters, Development of micromechanical models for granular media, Granular Matter **9**, 337 (2007).

[3] N. W. Hayman, L. Ducloué, K. L. Foco, and K. E. Daniels, Granular controls on periodicity of stick-slip events: Kinematics and force-chains in an experimental fault, Pure Appl. Geophys. **168**, 2239 (2011).

[4] L. Zhang, Y. Wang, and J. Zhang, Force-chain distributions in granular systems, Phys. Rev. E **89**, 012203 (2014).

[5] C. Zhai, E. B. Herbold, and R. C. Hurley, The influence of packing structure and interparticle forces on ultrasound transmission in granular media, Proc. Natl. Acad. Sci. USA **117**, 16234 (2020).

[6] E. T. Owens and K. E. Daniels, Sound propagation and force chains in granular materials, Europhys. Lett. **94**, 54005 (2011).

[7] D. Bi, S. Henkes, K. E. Daniels, and B. Chakraborty, The statistical physics of athermal materials, Annu. Rev. Condens. Matter Phys. **6**, 63 (2015).

[8] K. E. Daniels, J. E. Kollmer, and J. G. Puckett, Photoelastic force measurements in granular materials, Rev. Sci. Instrum. **88**, 051808 (2017).

[9] T. S. Majmudar and R. P. Behringer, Contact force measurements and stress-induced anisotropy in granular materials, Nature (London) **435**, 1079 (2005).

[10] E. I. Corwin, H. M. Jaeger, and S. R. Nagel, Structural signature of jamming in granular media, Nature (London) **435**, 1075 (2005).

[11] J. A. Dijksman, F. Rietz, K. A. Lőrincz, M. van Hecke, and W. Losert, Invited article: Refractive index matched scanning of dense granular materials, Rev. Sci. Instrum. **83**, 011301 (2012).

[12] N. Brodu, J. A. Dijksman, and R. P. Behringer, Spanning the scales of granular materials through microscopic force imaging, Nat. Commun. **6**, 6361 (2015).

[13] M. Saadatfar, A. P. Sheppard, T. J. Senden, and A. J. Kabla, Mapping forces in a 3d elastic assembly of grains, J. Mech. Phys. Solids **60**, 55 (2012).

[14] J. Brujić, S. F. Edwards, D. V. Grinev, I. Hopkinson, D. Brujić, and H. A. Makse, 3d bulk measurements of the force distribution in a compressed emulsion system, Faraday Discuss. **123**, 207 (2003).

[15] A. Kondo, D. Takano, E. Kohama, and R. J. Bathurst, Visualization and measurement of load transmission in granular assemblies using mechanoluminescent-coated particles, Granular Matter **21**, 50 (2019).

[16] M. Tolomeo, V. Richefeu, G. Combe, J. Roux, and G. Viggiani, An assessment of discrete element approaches to infer intergranular forces from experiments on 2d granular media, Int. J. Solids Struct. **187**, 48 (2020).
[17] R. C. Hurley, S. A. Hall, J. E. Andrade, and J. Wright, Quantifying Interparticle Forces and Heterogeneity in 3d Granular Materials, Phys. Rev. Lett. **117**, 098005 (2016).
[18] R. C. Hurley, J. Lind, D. C. Pagan, M. A. Homel, M. C. Akin, and E. B. Herbold, Linking initial microstructure and local response during quasistatic granular compaction, Phys. Rev. E **96**, 012905 (2017).
[19] R. Hurley, S. Hall, and J. Wright, Multi-scale mechanics of granular solids from grain-resolved x-ray measurements, Proc. R. Soc. A. **473**, 20170491 (2017).
[20] R. Hurley, J. Lind, D. Pagan, M. Akin, and E. Herbold, In situ grain fracture mechanics during uniaxial compaction of granular solids, J. Mech. Phys. Solids **112**, 273 (2018).
[21] R. C. Hurley, E. B. Herbold, and D. C. Pagan, Characterization of the crystal structure, kinematics, stresses and rotations in angular granular quartz during compaction, J. Appl. Crystallogr. **51**, 1021 (2018).
[22] C. Zhai, E. Herbold, S. Hall, and R. Hurley, Particle rotations and energy dissipation during mechanical compression of granular materials, J. Mech. Phys. Solids **129**, 19 (2019).
[23] C. Zhai, N. Albayrak, J. Engqvist, S. A. Hall, J. Wright, M. Majkut, E. B. Herbold, and R. C. Hurley, Quantifying local rearrangements in three-dimensional granular materials: Rearrangement measures, correlations, and relationship to stresses, Phys. Rev. E **105**, 014904 (2022).
[24] L. Li, E. Marteau, and J. E. Andrade, Capturing the interparticle force distribution in granular material using ls-dem, Granular Matter **21**, 43 (2019).
[25] E. Marteau and J. E. Andrade, A novel experimental device for investigating the multiscale behavior of granular materials under shear, Granular Matter **19**, 77 (2017).
[26] R. Hurley, K. Lim, G. Ravichandran, and J. Andrade, Dynamic inter-particle force inference in granular materials: method and application, Exp. Mech. **56**, 217 (2016).
[27] H. Kocharyan and N. Karanjgaokar, Influence of lateral constraints on wave propagation in finite granular crystals, J. Appl. Mech. **87**, 071011 (2020).
[28] J. E. Andrade and C. F. Avila, Granular element method (gem): Linking inter-particle forces with macroscopic loading, Granular Matter **14**, 51 (2012).
[29] R. Hurley, E. Marteau, G. Ravichandran, and J. E. Andrade, Extracting inter-particle forces in opaque granular materials: Beyond photoelasticity, J. Mech. Phys. Solids **63**, 154 (2014).
[30] R. C. Hurley, Stress and force measurement uncertainties in 3D granular materials, EPJ Web Conf. **249**, 02009 (2021).
[31] C. Zhai, D. Pagan, and R. Hurley, In situ x-ray tomography and 3d x-ray diffraction measurements of cemented granular materials, JOM **72**, 18 (2020).
[32] S. Boyd, S. P. Boyd, and L. Vandenberghe, *Convex Optimization* (Cambridge University, New York, 2004).
[33] J. Oddershede, S. Schmidt, H. F. Poulsen, H. O. Sørensen, J. Wright, and W. Reimers, Determining grain resolved stresses in polycrystalline materials using three-dimensional x-ray diffraction, J. Appl. Crystallogr. **43**, 539 (2010).
[34] J. V. Bernier, N. R. Barton, U. Lienert, and M. P. Miller, Far-field high-energy diffraction microscopy: A tool for intergranular orientation and strain analysis, J. Strain Anal. Eng. **46**, 527 (2011).
[35] M. A. Sutton, J. J. Orteu, and H. Schreier, *Image Correlation for Shape, Motion and Deformation Measurements: Basic Concepts, Theory and Applications* (Springer, New York, 2009).
[36] S. Weis and M. Schröter, Analyzing x-ray tomographies of granular packings, Rev. Sci. Instrum. **88**, 051809 (2017).
[37] M. Wiebicke, E. Andò, I. Herle, and G. Viggiani, On the metrology of interparticle contacts in sand from x-ray tomography images, Meas. Sci. Technol. **28**, 124007 (2017).
[38] E. Ando, Experimental investigation of microstructural changes in deforming granular media using x-ray tomography, Ph.D. thesis, Université de Grenoble, 2013.
[39] K. Senetakis, M. R. Coop, and M. C. Todisco, The inter-particle coefficient of friction at the contacts of leighton buzzard sand quartz minerals, Soils and Foundations **53**, 746 (2013).
[40] C. Kloss, C. Goniva, A. Hager, S. Amberger, and S. Pirker, Models, algorithms and validation for opensource DEM and CFD-DEM, Prog. Comput. Fluid Dyn. Int. J. **12**, 140 (2012).
[41] E. R. Dobrovinskaya, L. A. Lytvynov, and V. Pishchik, *Sapphire: Material, Manufacturing, Applications* (Springer, New York, 2009).
[42] A. Tordesillas, Force chain buckling, unjamming transitions and shear banding in dense granular assemblies, Philos. Mag. **87**, 4987 (2007).
[43] A. Tordesillas and M. Muthuswamy, On the modeling of confined buckling of force chains, J. Mech. Phys. Solids **57**, 706 (2009).
[44] H. Poulsen, *Three-Dimensional X-Ray Diffraction Microscopy: Mapping Polycrystals and Their Dynamics* (Springer, New York, 2004).